



# 1 **Impact of mineral dust on the global nitrate aerosol direct and** 2 **indirect radiative effect**

3 Alexandros Milousis<sup>1</sup>, Klaus Klingmüller<sup>2</sup>, Alexandra P. Tsimpidi<sup>1</sup>, Jasper F. Kok<sup>3</sup>, Maria  
4 Kanakidou<sup>4,5,6</sup>, Athanasios Nenes<sup>5,7</sup>, and Vlassis A. Karydis<sup>1</sup>

5 <sup>1</sup>Institute for Energy and Climate Research, IEK-8 Troposphere, Forschungszentrum Jülich GmbH, Jülich, Germany

6 <sup>2</sup>Max Planck Institute for Chemistry, Mainz, Germany

7 <sup>3</sup>Department of Atmospheric and Oceanic Sciences, University of California Los Angeles, Los Angeles, CA, USA.

8 <sup>4</sup>Environmental Chemical Processes Laboratory, Department of Chemistry, University of Crete, Heraklion, Greece

9 <sup>5</sup>Center for the Study of Air Quality and Climate Change, Foundation for Research & Technology Hellas, Patras,  
10 Greece

11 <sup>6</sup>Institute of Environmental Physics, University of Bremen, Bremen, Germany

12 <sup>7</sup>Laboratory of Atmospheric Processes and Their Impacts, Ecole Polytechnique Fédérale de Lausanne, Switzerland

13 *Correspondence to:* Vlassis A. Karydis (v.karydis@fz-juelich.de)

## 14 **Abstract**

15 Nitrate (NO<sub>3</sub><sup>-</sup>) aerosol is projected to increase dramatically in the coming decades and may become the  
16 dominant inorganic particle species. This is due to the continued strong decrease in SO<sub>2</sub> emissions, which  
17 is not accompanied by a corresponding decrease in NO<sub>x</sub> and especially NH<sub>3</sub> emissions. Thus, the radiative  
18 effect (RE) of NO<sub>3</sub><sup>-</sup> aerosol may become more important than that of SO<sub>4</sub><sup>2-</sup> aerosol in the future. The  
19 physicochemical interactions of mineral dust particles with gas and aerosol tracers play an important role  
20 in influencing the overall RE of dust and non-dust aerosols but can be a major source of uncertainty due to  
21 their lack of representation in many global climate models. Therefore, this study investigates how and to  
22 what extent dust affects the current global NO<sub>3</sub><sup>-</sup> aerosol radiative effect through both radiation (RE<sub>ari</sub>) and  
23 cloud interactions (RE<sub>aci</sub>) at the top of the atmosphere (TOA). For this purpose, multi-year simulations  
24 nudged towards the observed atmospheric circulation were performed with the global atmospheric  
25 chemistry and climate model EMAC, while the thermodynamics of the interactions between inorganic  
26 aerosols and mineral dust were simulated with the thermodynamic equilibrium model ISORROPIA-lite.  
27 The emission flux of the mineral cations Na<sup>+</sup>, Ca<sup>2+</sup>, K<sup>+</sup> and Mg<sup>2+</sup> is calculated as a fraction of the total  
28 aeolian dust emission based on the unique chemical composition of the major deserts worldwide. Our  
29 results reveal positive and negative shortwave and longwave radiative effects in different regions of the  
30 world via aerosol-radiation interactions and cloud adjustments. Overall, the NO<sub>3</sub><sup>-</sup> aerosol direct effect  
31 contributes a global cooling of -0.11 W/m<sup>2</sup>, driven by coarse-mode particle cooling at short wavelengths.  
32 Regarding the indirect effect, it is noteworthy that NO<sub>3</sub><sup>-</sup> aerosol exerts a global mean warming of +0.17  
33 W/m<sup>2</sup>. While the presence of NO<sub>3</sub><sup>-</sup> aerosol enhances the ability of mineral dust particles to act as cloud  
34 condensation nuclei (CCN), it simultaneously inhibits the formation of cloud droplets from the smaller  
35 anthropogenic particles. This is due to the coagulation of fine anthropogenic CCN particles with the larger  
36 nitrate-coated mineral dust particles, which leads to a reduction in total aerosol number concentration. This  
37 mechanism results in an overall reduced cloud albedo effect and is thus attributed as warming.

38

39 **Keywords:** direct radiative effect, indirect radiative effect, nitrate aerosols, mineral dust

40



## 41 1. Introduction

42 Atmospheric aerosols are among the most complex components of the Earth's climate system.  
43 This is due not only to the diversity of their origins, with many natural and anthropogenic emission  
44 sources, but also to their extremely varied chemical composition and properties. The many  
45 mechanisms by which they interact with each other and with physical entities such as radiation,  
46 clouds, land, and oceans add to their complexity and play a critical role in the energy balance of  
47 the planet (Arias et al., 2021). The most direct way in which aerosols affect the Earth's energy  
48 balance is through their interactions with solar shortwave (SW) and terrestrial longwave (LW)  
49 radiation (IPCC, 2013). Overall, the radiative effect due to aerosol-radiation interactions ( $RE_{\text{ari}}$ ) is  
50 mainly dominated by the scattering of SW radiation back to space (negative radiative effect,  
51 generating a cooling of the climate system) and the absorption of LW radiation (positive radiative  
52 effect, generating a warming of the climate system) (Gao et al., 2018; Tsigaridis and Kanakidou,  
53 2018). Aerosols belonging to the black and/or brown carbon family, together with mineral dust  
54 particles, contribute to absorption (Kanakidou et al., 2005; Zhang et al., 2017; Wong et al., 2019),  
55 while the main inorganic aerosol components, such as sulfate and nitrate, as well as a significant  
56 amount of organic carbon contribute mainly to scattering (Kirchstetter et al., 2004; (Bond and  
57 Bergstrom, 2006; Klingmüller et al., 2019; Zhang, 2020). However, mineral dust can also  
58 influence the behavior of the  $RE_{\text{ari}}$  of anthropogenic pollution. Dust particles alter the  
59 anthropogenic radiative effect of aerosol-radiation interactions by reducing the loading of  
60 anthropogenic aerosols (either by coagulating with them or by adsorption of their precursor  
61 inorganic trace gases), leading to less scattering of solar radiation and thus a warming effect (Kok  
62 et al., 2023).

63 Atmospheric aerosols can also indirectly affect the Earth's energy balance by forming clouds,  
64 controlling cloud optical thickness and scattering properties, and altering their precipitation and  
65 lifetime (IPCC, 2013). Atmospheric aerosols act as cloud condensation nuclei (CCN), providing a  
66 suitable surface for water vapor to condense, leading to the formation of liquid droplets that  
67 develop into a corresponding liquid cloud (Lance et al., 2004). Such clouds are referred to as warm  
68 clouds and are typically found in the lower troposphere (Khain and Pinsky, 2018). However, there  
69 is constant competition between small and large particles for the available amount of water vapor  
70 (Barahona et al., 2010; Morales and Nenes, 2014). Under the same humidity conditions, the  
71 presence of small particles will lead to the formation of small droplets with high number  
72 concentrations, while the presence of larger particles will lead to the formation of large droplets  
73 but with lower number concentrations. Depending on the size characteristics of its particle  
74 population, a warm cloud will exhibit different optical properties, with a population dominated by  
75 smaller particles generally being more reactive in the SW spectrum. The change in cloud  
76 reflectivity due to the presence of aerosols is referred to as the first radiative effect due to aerosol-  
77 cloud interactions ( $RE_{\text{aci}}$ ) and was first described by Twomey (1977). The small size of  
78 anthropogenic aerosols results in an overall smaller cloud droplet size, which reduces precipitation  
79 efficiency and thus increases cloud lifetime. This contributes to cloud reflectivity and is referred  
80 to as the second radiative effect of aerosol cloud-interactions, first described by Albrecht (1989).  
81 These two indirect effects are considered equally important for the total indirect radiative effect of  
82 aerosols (Lohmann and Feichter, 2005). Atmospheric aerosols exert a net cooling effect that can  
83 partially mask the warming effect of greenhouse gases, therefore, the recent decline in



84 anthropogenic aerosol concentrations may accelerate global warming (Urdiales-Flores et al.,  
85 2023). Overall, the radiative effect due to aerosol-cloud interactions is considered the main source  
86 of existing uncertainty in the effective (total) radiative effect of aerosols in the atmosphere (Myhre  
87 et al., 2014; Seinfeld et al., 2016).

88 Mineral dust influences the anthropogenic radiative effect through aerosol-cloud interactions in  
89 several ways that can result in either a net warming or net cooling effect. Dust particles can increase  
90 the number of CDNC in remote areas since through chemical aging by pollutants (Nenes et al.,  
91 2014; Karydis et al., 2017), dust particles become more hygroscopic and require lower  
92 supersaturation thresholds for activation (Karydis et al., 2011). This is caused by the transfer of  
93 anthropogenic pollutants towards remote desert regions which enhances the solubility of dust  
94 particles. In such regions, this mostly results in increased cloud albedo and a net cooling effect.  
95 However, dust particles also tend to reduce the availability of smaller anthropogenic CCN. This is  
96 due to intrusions of aged dust particles into polluted environments which reduce the numbers of  
97 smaller aerosols through increased coagulation with them. This results in lower cloud reflectivity  
98 (albedo) and thus a net warming effect (Klingmüller et al., 2020). Furthermore, when dust is above  
99 or below low-level clouds, the resulting effect of local heating is an increase in total cloud cover  
100 due to enhanced temperature inversion or enhanced upward vertical motion, respectively (Kok et  
101 al., 2023). On the other hand, when dust is present inside low-level clouds, local heating enhances  
102 in-cloud evaporation, resulting in an overall decrease in cloud cover. Kok et al. (2023) showed that  
103 the amount of desert dust in the atmosphere has increased since the mid-19<sup>th</sup> century, causing an  
104 overall cooling effect on the Earth that masks up to 8% of the warming caused by greenhouse  
105 gases. If the increase in dust were halted, the previously hidden additional warming potential of  
106 greenhouse gases could lead to slightly faster climate warming.

107  $\text{NO}_3^-$  is expected to dominate the global aerosol composition in the coming decades due to the  
108 predicted limited availability of  $\text{SO}_4^{2-}$  following the abrupt decline in  $\text{SO}_2$  emissions, which will  
109 not necessarily be accompanied by proportional reductions in  $\text{NO}_x$  and  $\text{NH}_3$  emissions (Bellouin  
110 et al., 2011; Hauglustaine et al., 2014). Excess  $\text{NO}_3^-$  is expected to exert a cooling  $\text{RE}_{\text{ari}}$  by  
111 scattering SW radiation (Bauer et al., 2007a; Xu and Penner, 2012; Myhre et al., 2013; IPCC,  
112 2013; Li et al., 2015), but the  $\text{RE}_{\text{aci}}$  is much more complex and complicated and can lead to both  
113 cooling and warming. Mineral dust thus becomes a key factor, as it is one of the main promoters  
114 of  $\text{NO}_3^-$  aerosol formation, providing a very suitable surface for gaseous  $\text{HNO}_3$  condensation to  
115 the aerosol phase (Karydis et al., 2011; Trump et al., 2015). This affects not only the optical  
116 properties of dust aerosols, which will influence their overall  $\text{RE}_{\text{ari}}$ , but also how they can alter  
117 cloud formation and microphysics.  $\text{NO}_3^-$  aerosols increase the hygroscopicity of mineral dust  
118 (Kelly et al., 2007) by providing layers of soluble material on their surface, thus increasing their  
119 ability to act as CCN (Karydis et al., 2017). In doing so, they also increase the size of dust particles  
120 through hygroscopic growth and therefore their coagulation efficiency. Thus, nitrate-dust  
121 interactions are a complex mechanism that ultimately affects climatology in a variety of ways. The  
122 role of mineral dust in modifying the influence of  $\text{NO}_3^-$  aerosols in the global  $\text{RE}_{\text{aci}}$  is not yet well  
123 understood. This study aims to focus on the extent of the  $\text{RE}_{\text{ari}}$  and  $\text{RE}_{\text{aci}}$  of  $\text{NO}_3^-$  aerosols and on  
124 how interactions with mineral dust regulate both on a global scale.

125 This study is organized as follows: in Section 2, details of the modeling setup for conducting  
126 the global simulations as well as the treatment of dust-nitrate interactions in the model are



127 discussed and the methodology for calculating the global  $RE_{ari}$  and  $RE_{aci}$  of  $NO_3^-$  aerosols is  
 128 explained. Section 3 presents the main results for the global  $RE_{ari}$  for coarse and fine  $NO_3^-$  aerosols  
 129 for the base case simulation and the sensitivity cases listed in Table 1. Section 4 presents the results  
 130 for the global  $RE_{aci}$  of total  $NO_3^-$  aerosols, while section 5 includes the feedback mechanism of  
 131 dust-nitrate interactions with cloud microphysics. Finally, the main conclusions and a general  
 132 discussion on the scope of the study are presented in section 6.

133 **Table 1:** Differences between base case and sensitivity simulations performed.

Simulation Name	Conditions Applied
Base Case	Mineral dust ion composition according to Karydis et al. (2016)
<u>Sensitivity 1:</u> Chemically Inert Dust	Mineral dust emitted exclusively as a chemically inert bulk particle
<u>Sensitivity 2:</u> Homogeneous Ion Composition	Global homogeneous ionic composition of mineral dust particles according to Sposito (1989)
<u>Sensitivity 3:</u> Half Dust Scenario	50% reduced dust emission flux.
<u>Sensitivity 4:</u> Increased Dust Scenario	50% increased dust emission flux.

134 **2. Methodology**

135 **2.1 Model Setup**

136 The simulations were performed with the global atmospheric chemistry and climate model  
 137 EMAC (ECHAM/MESSy) (Jockel et al., 2006), which includes several submodels describing  
 138 atmospheric processes and their interactions with oceans, land, and human influences. These  
 139 submodels are linked through the Modular Earth Submodel System (MESSy) (Jockel et al., 2005)  
 140 to a base model, the 5<sup>th</sup> Generation European Center Hamburg General Circulation Model  
 141 (ECHAM) (Roeckner et al., 2006). The submodel system used in this work includes the MECCA  
 142 submodel, which performs the gas phase chemistry calculations (Sander et al., 2019). The SCAV  
 143 submodel is responsible for the in-cloud liquid-phase chemistry and wet deposition processes (Tost  
 144 et al., 2006; Tost et al., 2007b), while DRYDEP and SEDI are used to compute the dry deposition  
 145 of gases and aerosols and gravitational settling, respectively (Kerkweg et al., 2006). All aerosol



146 microphysical processes are calculated by the GMXe submodel (Pringle et al., 2010a; Pringle et  
147 al., 2010b), where aerosols are divided into 4 lognormal size modes (nucleation, Aitken,  
148 accumulation and coarse). Each mode is defined in terms of aerosol number concentration, number  
149 mean dry radius, and geometric standard deviation ( $\sigma$ ). The mean dry radius for each mode is  
150 allowed to vary within fixed bounds (0.5 nm – 6 nm for nucleation, 6 nm - 60 nm for Aitken, 60  
151 nm - 700 nm for accumulation, and above 700 for coarse) and the  $\sigma$  is fixed and equal to 1.59  
152 for the first three size modes and 2 for the coarse mode. The coagulation of aerosols is also handled  
153 by GMXe, following Vignati et al. (2004) and the coagulation coefficients for Brownian motion  
154 are calculated according to Fuchs and Davies (1964). The partitioning between the gas and aerosol  
155 phases is calculated using the ISORROPIA-lite thermodynamic module (Kakavas et al., 2022) as  
156 implemented in EMAC by Milousis et al. (2024). The optical properties of the aerosols and the  
157 radiative transfer calculations are simulated by the submodels AEROPT (Dietmuller et al., 2016)  
158 and RAD (Dietmuller et al., 2016), respectively. AEROPT can be called several times within a  
159 model time step with different settings for the aerosol properties. More details are given in section  
160 2.3.1. All cloud properties and microphysical processes are simulated by the CLOUD submodel  
161 (Roeckner et al., 2006) using the two-moment microphysical scheme of Lohmann and Ferrachat  
162 (2010) for liquid and ice clouds. The activation processes of liquid cloud droplets and ice crystals  
163 follow the physical treatment of Morales and Nenes (2014) and Barahona and Nenes (2009),  
164 respectively, as described by Karydis et al. (2017) and Bacer et al. (2018). More details are given  
165 in Section 2.3.2.

166 The meteorology for each of the simulations was nudged by ERA5 reanalysis data (C3S, 2017),  
167 thus this study estimates the radiative effect of nitrate aerosols with respect to  $RE_{ari}$  and  $RE_{aci}$   
168 separately, rather than the effective (total) radiative effect, as this would require multiple free-run  
169 simulations with prescribed sea surface temperatures for each case separately. The spectral  
170 resolution used for each simulation was T63L31, which corresponds to a grid resolution of  $1.875^\circ$   
171  $\times 1.875^\circ$  and 31 vertical layers up to 25 km in height. The period covered by the simulations is  
172 from 2007 to 2018, with the first year representing the model spin-up period.

173 Anthropogenic aerosol and trace gas emissions were taken from the CMIP6 database (O'Neill  
174 et al., 2016) according to the SSP370 scenario. Natural  $NH_3$  emissions (from land and ocean) were  
175 based on the GEIA database (Bouwman et al., 1997), and natural volcanic  $SO_2$  emissions were  
176 taken from the AEROCOM database (Dentener et al., 2006). Biogenic  $NO$  emissions from soils  
177 were calculated online according to the algorithm of Yienger and Levy (1995), while lightning-  
178 produced  $NO_x$  was also calculated online by the LNO<sub>x</sub> submodel (Tost et al., 2007a) using the  
179 parameterization of Grewe et al. (2001). DMS emissions from the oceans are calculated online by  
180 the AIRSEA submodel (Pozzer et al., 2006). Sea salt emissions are based on the AEROCOM  
181 database (Dentener et al., 2006) following the chemical composition reported by Seinfeld and  
182 Pandis (2016), i.e. 30.6%  $Na^+$ , 3.7%  $Mg^{2+}$ , 1.2%  $Ca^{2+}$ , 1.1%  $K^+$ , and 55%  $Cl^-$ . Dust emissions are  
183 calculated online using the parameterization of Astitha et al. (2012). In this scheme, while the  
184 surface friction velocity is the most important parameter for the amount of the emitted dust flux,  
185 the meteorological information for each grid cell is also taken into account. Dust particles are  
186 emitted in the accumulation and coarse size modes of the insoluble fraction, but can be transferred  
187 to the soluble fraction after either coagulation with other soluble species and/or by condensation  
188 of soluble material on their surface. Both processes are treated and calculated by GMXe and



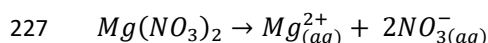
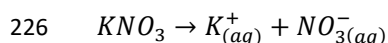
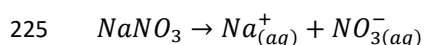
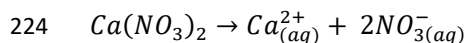
189 ISORROPIA-lite. The emissions of mineral ions ( $\text{Ca}^{2+}$ ,  $\text{Mg}^{2+}$ ,  $\text{K}^+$ , and  $\text{Na}^+$ ) are estimated as a  
190 fraction of the total dust emission flux based on the soil chemical composition of each grid cell.  
191 This is done using desert soil composition maps from Klingmüller et al. (2018) which are based  
192 on the mineral ion fractions from Karydis et al. (2016). To assess the impact of changes in mineral  
193 dust chemistry and emissions on the global  $\text{NO}_3^-$  aerosol  $\text{RE}_{\text{ari}}$  and  $\text{RE}_{\text{aci}}$ , four additional sensitivity  
194 simulations were performed (Table 1). In the first sensitivity simulation, mineral dust is described  
195 only by a bulk, chemically inert species. In the second sensitivity case, the chemical composition  
196 of the mineral dust was assumed to be spatially uniform, with a percentage distribution for bulk  
197 dust,  $\text{Na}^+$ ,  $\text{K}^+$ ,  $\text{Ca}^{2+}$  and  $\text{Mg}^{2+}$  particles assumed to be 94%, 1.2%, 1.5%, 2.4% and 0.9%  
198 respectively according to Sposito (1989). Finally, two additional simulations were performed to  
199 assess the impact of the global mineral dust budget on the results, where the dust emission fluxes  
200 were first halved and then increased by 50% to account for the historical increase in global dust  
201 mass load since pre-industrial times, as reconstructed by Kok et al. (2023).

202

## 203 **2.2 Treatment of Dust-Nitrate Interactions**

204 The interactions between mineral dust and nitrate aerosols play a crucial role in altering the size  
205 distribution and optical properties of both species and can also strongly influence cloud  
206 microphysical processes (Fig. 1). Therefore, these interactions affect both the  $\text{RE}_{\text{ari}}$  and the  $\text{RE}_{\text{aci}}$   
207 of both nitrate and dust aerosols. First, the adsorption of  $\text{HNO}_3$  onto the surface of dust particles  
208 is a process that strongly promotes the formation of nitrate aerosols on dust (Karydis et al., 2016).  
209 We treat this condensation process using the GMXe submodel. Specifically, the amount of gas  
210 phase species that kinetically condenses within a model time step (equal to 10 minutes in this  
211 study) is calculated according to the diffusion-limited condensation theory of Vignati et al. (2004).  
212 This information is then passed to the ISORROPIA-lite thermodynamic module to calculate the  
213 gas/aerosol partitioning.

214 Specifically, the module receives as input the ambient temperature and humidity along with the  
215 diffusion-limited concentrations of  $\text{H}_2\text{SO}_4$ ,  $\text{NH}_3$ ,  $\text{HNO}_3$ , and  $\text{HCl}$ , the concentrations of the non-  
216 volatile cations (NVCs)  $\text{Na}^+$ ,  $\text{K}^+$ ,  $\text{Ca}^{2+}$  and  $\text{Mg}^{2+}$ , and the concentrations of the ions  $\text{SO}_4^{2-}$ ,  $\text{NO}_3^-$ ,  
217  $\text{NH}_4^+$ , and  $\text{Cl}^-$  present in the aerosol phase from the previous time step. The module then calculates  
218 the equilibrium reactions of the  $\text{NO}_3^-$  anion with the NVCs, depending on their abundance with  
219 respect to the  $\text{SO}_4^{2-}$  anion, taking into account mass conservation, electroneutrality, water activity  
220 equations and precalculated activity coefficients for specific ionic pairs (Fountoukis et al., 2007;  
221 Kakavas et al., 2022). Therefore, in all cases where mineral dust is considered chemically active,  
222 all reactions of nitrate aerosols with NVC are treated. The salts that may be formed are assumed  
223 to be completely deliquesced as follows:



228

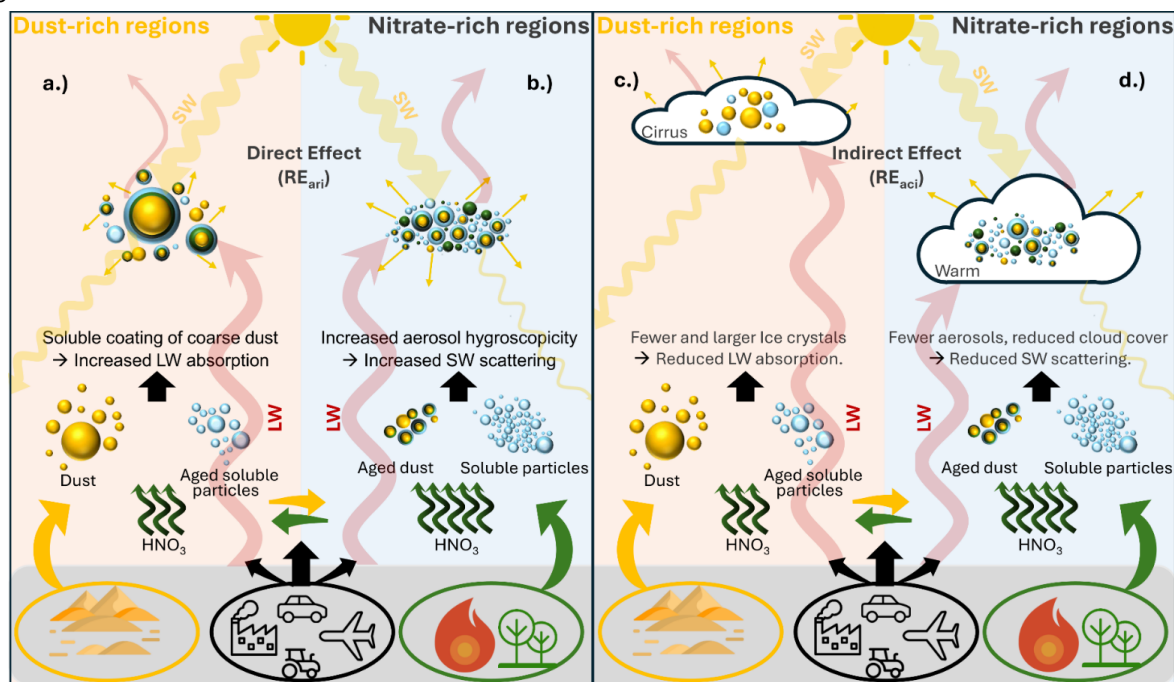




229 More information on equilibrium reactions and equilibrium constants as well as the corresponding  
 230 thermodynamic equilibrium calculations can be found in Fountoukis and Nenes (2007).

231 The coating of dust particles by nitrate aerosols during gas/aerosol partitioning calculations is  
 232 an important process that leads to an increase in dust solubility and hygroscopicity (Laskin et al.,  
 233 2005). Therefore, after these processes have taken place, a large fraction of the originally insoluble  
 234 dust particles has become soluble (Fig. 1a), which leads to changes in their optical properties, as  
 235 their increased ability to absorb water makes them more efficient in extinguishing SW radiation  
 236 and absorbing and emitting LW radiation (Fig. 1a, 1b) (Kok et al., 2023). The transfer to the soluble  
 237 fraction after coating with soluble material is handled by the GMXe submodel, which also provides  
 238 key aerosol attributes necessary for the calculation of the dust optical properties (see Section 2.3).

239



240 **Figure 1:** Conceptual illustration of how dust-nitrate interactions affect the total NO<sub>3</sub><sup>-</sup> (left) RE<sub>ari</sub> and  
 241 (right) RE<sub>aci</sub>. **a.)** In dust-rich environments, nitric acid transported from anthropogenic pollution and biomass  
 242 burning regions interacts with mineral cations to form a soluble coating on the surface of dust particles. The  
 243 dominant effect of these interactions is an enhanced LW absorption (warming RE<sub>ari</sub>) by the coarse dust  
 244 particles. **b.)** In nitrate-rich environments, the intrusion of dust particles and their subsequent interaction  
 245 with freshly emitted nitric acid leads to an overall increase in aerosol hygroscopicity and thus a stronger  
 246 SW reflection (cooling RE<sub>ari</sub>). **c.)** In dust-rich environments, the number of ice crystals in cirrus clouds is  
 247 reduced while their size is increased due to the interaction of dust particles with the transported HNO<sub>3</sub>. This  
 248 results in an optical thinning of the ice clouds, which leads to less trapping of outgoing LW radiation  
 249 (cooling RE<sub>aci</sub>). **d.)** In nitrate-rich environments, the increased wet radius of aged dust particles leads to  
 250 enhanced coagulation with smaller particles, resulting in a decrease in the number of smaller aerosols and,  
 251 in turn, a decrease in the number of activated particles in cloud droplets by smaller aerosols, which  
 252 ultimately leads to a reduction in the backscattering of SW radiation by warm clouds (warming RE<sub>ari</sub>).



253 In general, the changes in the properties of dust particles through their interactions with nitrate  
254 aerosols will result in more efficient removal rates, mainly through wet deposition, due to their  
255 higher hygroscopicity and increased size (Fan et al., 2004). The reduced number of dust particles  
256 that can act as ice nuclei (IN) and their increased size can lead to an optical thinning of cirrus  
257 clouds (Fig. 1c) (Kok et al., 2023). Furthermore, the changes induced by dust-nitrate interactions  
258 reduce the activation of smaller aerosols in warm clouds (Fig. 1d). In particular, the enhanced  
259 hygroscopicity of dust particles will lead to a faster depletion of the available supersaturation, as  
260 they act as giant CCN that absorb large amounts of water vapor to activate into cloud droplets  
261 (Karydis et al., 2017). In addition, the population of smaller aerosols will also be depleted by  
262 increased coagulation with the large dust particles. As a consequence of the different degrees of  
263 complexity of the dust-nitrate interactions, it is very important to note that they do not always  
264 result in a linear response in terms of how they affect climate through their subsequent interactions  
265 with radiation, clouds, or both.  
266

## 267 **2.3 Radiative Effect Calculation**

268 To calculate the global  $RE_{ari}$  and  $RE_{aci}$  of  $NO_3^-$  aerosols, the optical properties from the  
269 AEROPT submodel and the radiative transfer calculations from the RAD submodel were used.  
270 First, AEROPT provides the aerosol extinction (absorption and scattering) coefficients, the single  
271 scattering albedo, and the aerosol asymmetry factor for each grid cell with a vertical distribution  
272 analogous to the vertical resolution used. The GMXe submodel is used to provide input of aerosol  
273 attributes for the calculation of aerosol optical properties, which is done online using 3D look-up  
274 tables. The tables provide information on the real and imaginary parts of the refractive index and  
275 the Mie size parameter per size mode (Dietmuller et al., 2016). Then, the radiative scheme of RAD  
276 uses the particle number weighted average of the extinction cross section, the single scattering  
277 albedo, and the asymmetry factor as input for the radiative transfer calculations. In addition to  
278 AEROPT, RAD takes input from the submodels ORBIT (Earth orbital parameters), CLOUDOPT  
279 (cloud optical properties) (Dietmuller et al., 2016), and IMPORT (import of external datasets) to  
280 calculate the radiative transfer properties for longwave and shortwave radiation fluxes separately.  
281 Both the AEROPT and RAD submodels can be invoked multiple times within a model time step,  
282 each time with different settings for the aerosol optical properties, allowing radiative transfer  
283 estimates for identical climatological conditions. This is of paramount importance for the  
284 calculation of the  $RE_{ari}$  of aerosols since any effects due to possibly different climatological  
285 conditions must be eliminated. Henceforth, all references to RE estimates, as well as net,  
286 longwave, and shortwave flux quantities, will refer to the top of the atmosphere (TOA) only.

### 287 **2.3.1 Radiative Effect from Aerosol-Radiation Interactions ( $RE_{ari}$ )**

288 To estimate the global  $RE_{ari}$  of all aerosols as well as that of total, coarse, and fine  $NO_3^-$  aerosols,  
289 3 simulations were performed for each sensitivity case in Table 1. In the first simulation all aerosol  
290 species are present, in the second simulation  $NO_3^-$  aerosols are completely removed by turning off  
291 their formation, and in the third simulation coarse mode  $NO_3^-$  aerosols are removed by forcing  
292  $HNO_3$  to condense only on the fine mode (i.e., sum of the three smaller lognormal size modes:  
293 nucleation, Aitken, and accumulation). For each of these three simulations, the radiative transfer  
294 routines are called twice for each time step. One call uses the normal aerosol optical properties,  
295 and the other call uses an aerosol optical depth equal to 0 to emulate an atmosphere without





296 aerosols. Essentially, the global  $RE_{ari}$  of each simulation can be calculated by taking the difference  
297 between the net fluxes between the two calls. More specifically, the first simulation will yield the  
298  $RE_{ari}$  of the total aerosol load ( $F_{1,ari}$  hereafter), the second simulation will yield the  $RE_{ari}$  of all  
299 aerosols except  $NO_3^-$  ( $F_{2,ari}$  below), and the third simulation will yield the  $RE_{ari}$  of all aerosols  
300 except the coarse mode  $NO_3^-$  ( $F_{3,ari}$  below). Since the above estimates of the radiative effect were  
301 computed using the exact same climatology, its effect was effectively eliminated. However, in  
302 order to isolate the  $NO_3^-$  aerosol radiative effect, it is also essential to disable any aerosol-cloud  
303 interactions, otherwise the cooling effect would be severely underestimated because cloud  
304 scattering would make aerosol scattering less relevant (Ghan et al., 2012). For this purpose, the  
305 simplest cloud scheme available in the EMAC model is used, which calculates cloud microphysics  
306 according to Lohmann and Roeckner (1996) and cloud coverage according to Tompkins (2002).  
307 To disable aerosol-cloud interactions, no aerosol activation routines are used to avoid coupling  
308 with the activation schemes. Overall, the global  $RE_{ari}$  of total, coarse, and fine  $NO_3^-$  aerosols are  
309 obtained as follows:

- 310 •  $F_{NO3,ari}(F_{N,ari}) = F_{1,ari} - F_{2,ari}$
- 311 •  $F_{coarseNO3,ari}(F_{cN,ari}) = F_{1,ari} - F_{3,ari}$
- 312 •  $F_{fineNO3,ari}(F_{fN,ari}) = F_{3,ari} - F_{2,ari}$

### 313 2.3.2 Radiative Effect from Aerosol-Cloud Interactions ( $RE_{aci}$ )

314 In this work we estimate the effect of total  $NO_3^-$  aerosols on the calculated global  $RE_{aci}$ .  
315 Climatology plays a crucial role in aerosol-cloud interactions and simulating a "fine-only  $NO_3^-$   
316 atmosphere", as done for the  $RE_{ari}$  calculations, would produce an unrealistic climatological  
317 scenario, since coarse-mode  $NO_3^-$  is strongly associated with cations in mineral dust particles  
318 (Karydis et al., 2016), making them quite effective as CCN (Karydis et al., 2017). Therefore, the  
319  $RE_{aci}$  calculations require only 2 simulations for each sensitivity case separately: one with all  
320 aerosols present and one with the entire  $NO_3^-$  aerosol load removed by turning off their formation.  
321 The global  $RE_{aci}$  is then given by:

- 322 •  $F_{NO3,aci}(F_{N,aci}) = FF_N - F_{N,ari}$

323 where  $FF_N$  is the total  $NO_3^-$  aerosol feedback radiative effect. Since  $F_{N,ari}$  is calculated using the  
324 methodology described in Section 2.3.1, it is only necessary to estimate  $FF_N$ . This is equal to the  
325 difference in net fluxes between the two simulations. There is no need to emulate an aerosol-free  
326 atmosphere here since any differences induced by different climatologies must be included. The  
327 two simulations performed for the calculation of  $RE_{aci}$  use the cloud formation scheme as described  
328 in Lohmann and Ferrachat (2010), which uses prognostic equations for the water phases and the  
329 bulk cloud microphysics. In addition, the empirical cloud cover scheme of Sundqvist et al. (1989)  
330 is used. For aerosol activation, the CDNC activation scheme of Morales and Nenes (2014) is used,  
331 which includes the adsorption activation of mineral dust as described in Karydis et al. (2017). The  
332 effect of dust-nitrate interactions on clouds presented here refers to the lowest level of cloud  
333 formation at 940 hPa. For the ICNC activation, the scheme of Barahona and Nenes (2009) is used,  
334 which calculates the ice crystal size distribution through heterogeneous and homogeneous freezing  
335 as well as ice crystal growth.



### 336 **3. Radiative Effect from Aerosol-Radiation Interactions ( $RE_{ari}$ )**

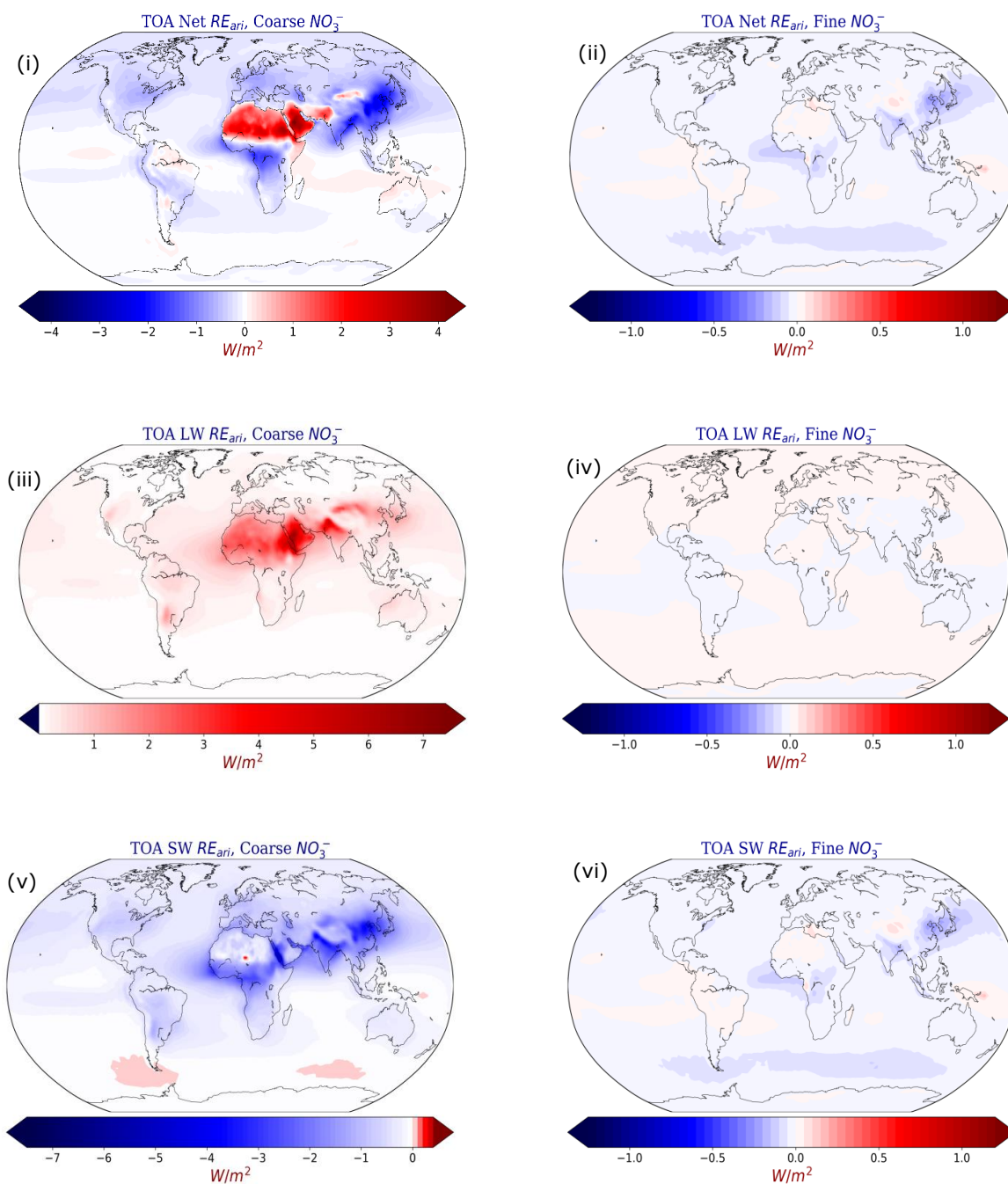
#### 337 **3.1 Base Case**

338 The global average  $RE_{ari}$  of total  $NO_3^-$  aerosols at the top of the atmosphere was found to be -  
339  $0.11 \text{ W/m}^2$ , which is within the reported range of the estimated present day all-sky direct radiative  
340 effect of total  $NO_3^-$  aerosols by other studies (Liao et al., 2004; Bauer et al., 2007a; Bauer et al.,  
341 2007b; Xu and Penner, 2012; Myhre et al., 2013; IPCC, 2013). The  $NO_3^-$  cooling of the  $RE_{ari}$   
342 calculated by EMAC is driven by the scattering of SW radiation (equal to  $-0.34 \text{ W/m}^2$ ), which  
343 outweighs the warming due to absorption of LW radiation (equal to  $+0.23 \text{ W/m}^2$ ) (Table 2). The  
344  $RE_{ari}$  of the total  $NO_3^-$  aerosol is dominated by the coarse particles, as they account for 82% of the  
345 calculated SW cooling and all the LW warming (Table 2; Figure 2). The warming effect of the  
346 coarse particles is strongest over the dust belt zone and especially over the regions of the Middle  
347 East and the northern face of the Himalayan plateau. These regions are characterized by high  
348 concentrations of coarse  $NO_3^-$  aerosols due to the adsorption of  $HNO_3$  on desert soil particles  
349 (Karydis et al., 2016; Milouis et al., 2024). Therefore, the warming due to absorption of terrestrial  
350 LW radiation by coarse-mode nitrates interacting with mineral dust is the strongest over these  
351 areas (Fig. 1a), reaching up to  $+4 \text{ W/m}^2$  (Fig. 2iii). On the other hand, the scattering of solar SW  
352 radiation is higher over regions with higher concentrations of total  $NO_3^-$  aerosols. Over the USA  
353 and Europe, the SW  $RE_{ari}$  is  $-1.5 \text{ W/m}^2$  (Fig. 2v). However, the cooling exerted by nitrate aerosol  
354 through the SW  $RE_{ari}$  is more profound over areas where it interacts strongly with high  
355 concentrations of mineral dust particles (Fig. 1b). Such areas include the Congo Basin, where  
356  $HNO_3$  from tropical forest biomass burning interacts with Saharan mineral dust particles; the North  
357 Indian region, where anthropogenic  $HNO_3$  emissions interact with mineral dust particles from the  
358 Taklimakan desert; and the East Asian region, where  $HNO_3$  emissions from Chinese megacities  
359 interact with mineral dust particles from the Gobi Desert. These regions can result in an average  
360 cooling of up to  $-4 \text{ W/m}^2$  (Fig. 2v).

361 Interestingly, cooling through SW interactions is not evident over the Sahara Desert, most likely  
362 due to the minimal presence of nitrate aerosols in the  $PM_{2.5}$  size range (not shown). The high  
363 concentrations of nitrate aerosols in the  $PM_{2.5-10}$  range over the Sahara contribute to LW  
364 absorption, but SW scattering is almost exclusively associated with the regions dominated by high  
365 concentrations in the  $PM_{2.5}$  (and smaller) size range (i.e. East Asia). Moreover, nitrate aerosols  
366 over the Sahara are exclusively associated with dust particles which have a relatively high  
367 imaginary part of the refractive index, with typical values for SW wavelengths being  $\sim 0.005$  (Di  
368 Biagio et al., 2019). As a result, nitrate aerosols over the Sahara exhibit relatively strong absorption  
369 in the SW spectrum as well, and the combination of the bright surface of the desert below leads to  
370 a weakened cooling effect and even sometimes in localized warming.

371 In contrast to the radiative effect of coarse  $NO_3^-$  particles, the  $RE_{ari}$  of fine  $NO_3^-$  particles due  
372 to interactions with LW radiation is negligible (Fig. 2iv), while its effect on SW radiation is about  
373 an order of magnitude smaller than that induced by the coarse  $NO_3^-$  aerosols (Fig. 2vi). The cooling  
374 induced by fine  $NO_3^-$  aerosols from the scattering of SW radiation is stronger over regions of high  
375 anthropogenic activity, namely the East Asian and Indian regions, which are characterized by high  
376 concentrations of fine  $NO_3^-$  aerosols, and peaks over eastern China ( $-0.25 \text{ W/m}^2$ ). Conversely, a  
377 weak warming effect ( $+0.15 \text{ W/m}^2$ ) is calculated over deserts (e.g. Gobi, Sahara).

378



379 **Figure 2:** Global mean TOA net  $RE_{ari}$  for (i) coarse and (ii) fine  $NO_3$  aerosols; longwave  $RE_{ari}$  for (iii)  
380 coarse and (iv) fine  $NO_3$  aerosols; shortwave  $RE_{ari}$  for (v) coarse and (vi) fine  $NO_3$  aerosols, as calculated  
381 by EMAC from the base case simulation.



382 **Table 2:** Net, longwave, and shortwave global mean TOA RE<sub>ari</sub> of total, coarse, and fine NO<sub>3</sub><sup>-</sup>  
 383 aerosols for the base case and each sensitivity case simulations.

384

385

Simulation	Aerosol Component	TOA RE <sub>ari</sub> (W/m <sup>2</sup> )		
		Net	LW	SW
<b>Base Case</b>	Total NO <sub>3</sub> <sup>-</sup>	- 0.11	+ 0.23	- 0.34
	Coarse NO <sub>3</sub> <sup>-</sup>	- 0.09	+ 0.23	- 0.32
	Fine NO <sub>3</sub> <sup>-</sup>	- 0.02	~ 0	- 0.02
<b>Chemically Inert Dust</b>	Total NO <sub>3</sub> <sup>-</sup>	- 0.09	+ 0.11	- 0.20
	Coarse NO <sub>3</sub> <sup>-</sup>	- 0.07	+ 0.11	- 0.18
	Fine NO <sub>3</sub> <sup>-</sup>	- 0.02	~ 0	- 0.02
<b>Homogeneous Ion Composition</b>	Total NO <sub>3</sub> <sup>-</sup>	- 0.09	+ 0.18	- 0.27
	Coarse NO <sub>3</sub> <sup>-</sup>	- 0.08	+ 0.18	- 0.26
	Fine NO <sub>3</sub> <sup>-</sup>	- 0.01	~ 0	- 0.01
<b>Half Dust Scenario</b>	Total NO <sub>3</sub> <sup>-</sup>	- 0.08	+ 0.19	- 0.27
	Coarse NO <sub>3</sub> <sup>-</sup>	- 0.06	+ 0.19	- 0.25
	Fine NO <sub>3</sub> <sup>-</sup>	- 0.02	~ 0	- 0.02
<b>Increased Dust Scenario</b>	Total NO <sub>3</sub> <sup>-</sup>	- 0.10	+ 0.27	- 0.37
	Coarse NO <sub>3</sub> <sup>-</sup>	- 0.08	+ 0.27	- 0.35
	Fine NO <sub>3</sub> <sup>-</sup>	- 0.02	~ 0	- 0.02

386



### 387 **3.2 Sensitivity of RE<sub>ari</sub> Estimates**

388 The comparison of the calculated total NO<sub>3</sub><sup>-</sup> radiative effect due to interactions with net, LW,  
389 and SW radiation for the sensitivity cases listed in Table 1 can be found in Table 2, which shows  
390 each of the estimates. Consideration of nitrate interactions with mineral dust cations can greatly  
391 affect the NO<sub>3</sub><sup>-</sup> RE<sub>ari</sub> estimates. Assuming that mineral dust particles are inert, the estimated  
392 warming due to LW radiation interactions is 52% weaker than in the base case where dust  
393 reactivity is considered. Similarly, the cooling effect exerted by nitrate aerosols through  
394 interactions with SW radiation is estimated to be 41% weaker under the assumption that mineral  
395 dust is non-reactive. Both estimates are lower when mineral dust is assumed to be chemically inert,  
396 since HNO<sub>3</sub> is no longer effectively adsorbed on dust particles and therefore the RE<sub>ari</sub> by coarse  
397 NO<sub>3</sub><sup>-</sup> aerosol is significantly weaker compared to the base case where it dominates the total NO<sub>3</sub><sup>-</sup>  
398 effect (see Sect. 3.1). However, since both the estimated warming and cooling are weaker, the  
399 effects partially cancel each other out, resulting in a net cooling effect (-0.09 W/m<sup>2</sup>) that is 18%  
400 weaker compared to the base case calculations. Assuming a homogeneous ionic composition for  
401 the dust, results in SW cooling and LW warming being 21% and 22% lower, respectively,  
402 weakening the estimate for the net cooling RE<sub>ari</sub> by 18% (-0.09 W/m<sup>2</sup>). The net direct radiative  
403 effect of total NO<sub>3</sub><sup>-</sup> is the same for the cases where dust is assumed to have a homogeneous  
404 chemical composition and where it has no chemical identity, indicating the importance of both  
405 aspects for the impact of dust-nitrate interactions on the direct radiative effect.

406 In the Half Dust scenario, the LW warming estimate is 17% weaker than in the base case, while  
407 the SW estimate is even more so (21%), resulting in a lower net cooling estimate of -0.08 W/m<sup>2</sup>.  
408 Finally, the Increased Dust scenario shows the strongest LW warming effect (17% increase over  
409 the base case) due to an increase in coarse mode nitrate. At the same time, the cooling effect due  
410 to interactions with SW radiation shows a smaller increase of 9%. Thus, accounting for the  
411 historical increase in mineral dust emissions results in a net cooling estimate of -0.10 W/m<sup>2</sup>, which  
412 is smaller than the base case. Interestingly, the behavior of the global total NO<sub>3</sub><sup>-</sup> RE<sub>ari</sub> does not  
413 exhibit linearity with respect to the global dust load. This is not surprising since the nitrate-dust  
414 interactions themselves are not linearly correlated, and a given increase or decrease in dust  
415 emissions does not lead to an analogous change in nitrate aerosol levels. For example, Karydis et  
416 al. (2016) have shown that moving from a scenario in which nitrate-dust chemistry is not  
417 considered to one in which it is, but with half dust emissions, resulted in a 39% increase in the  
418 tropospheric burden of nitrate aerosols. However, moving from a scenario with half to full dust  
419 emissions, the corresponding increase was only 9%. In our case, moving from the chemically inert  
420 dust scenario to the half dust scenario led to an 18% increase in atmospheric nitrate aerosol burden,  
421 while moving from the half dust scenario to the base case led to an additional 8% increase, and  
422 finally moving from the base case to the increased dust scenario led to an even smaller increase of  
423 5%.

## 424 **4 Radiative Effect from Aerosol-Cloud Interactions (RE<sub>aci</sub>)**

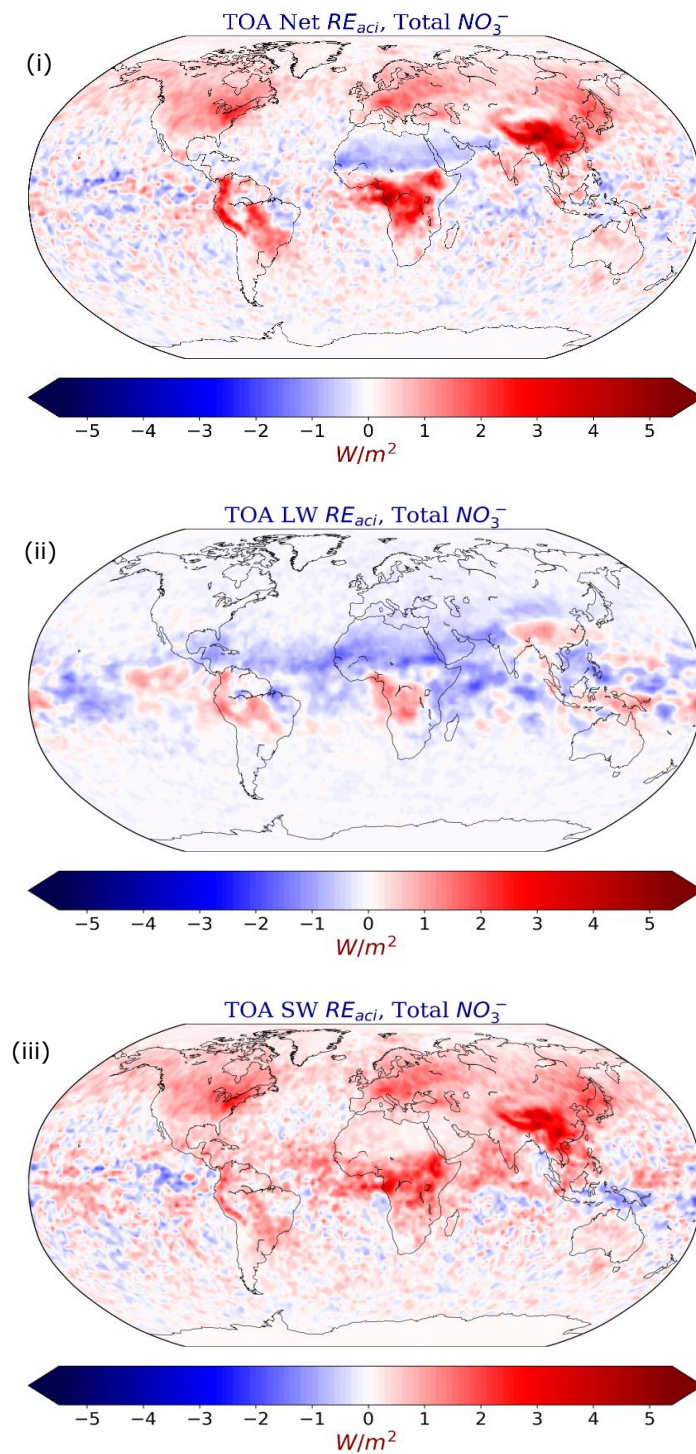
### 425 **4.1 Base Case**

426 The global average RE<sub>aci</sub> of total NO<sub>3</sub><sup>-</sup> aerosols at the top of the atmosphere was found to be  
427 +0.17 W/m<sup>2</sup>. In contrast, an estimate of the RE<sub>aci</sub> of nitrate aerosols by Xu and Penner (2012)  
428 showed only a trivial cooling effect for particulate NO<sub>3</sub><sup>-</sup> (-0.01 W/m<sup>2</sup>). Similar to the RE<sub>ari</sub>, the net





429  $RE_{aci}$  estimated by EMAC is driven by the effect on the SW part of the spectrum, which causes a  
430 warming effect of  $+0.27 \text{ W/m}^2$ , while the effect on the LW radiation causes an average cooling of  
431  $-0.10 \text{ W/m}^2$  (Table 3). Overall, the net  $RE_{aci}$  of total  $\text{NO}_3^-$  aerosols is reversed compared to the net  
432  $RE_{ari}$ , i.e.  $RE_{aci}$  exerts a strong cooling effect over regions where  $RE_{ari}$  exerts a warming effect and  
433 vice versa (Fig. 3i). The reason for this is that the regions contributing to a cooling  $RE_{ari}$  are  
434 dominated by smaller sized nitrate aerosols and vice versa. Therefore, the size characteristics of  
435 the dominant nitrate aerosol population lead to different effects on the cloud optical properties as  
436 discussed in section 1. For example, as the dominance of smaller nitrate aerosols decreases over a  
437 particular region, the optical thinning of low-level clouds will have an opposite effect on the  $RE_{aci}$   
438 (Fig. 1d). Details of the mechanism by which nitrate-dust interactions affect cloud microphysical  
439 processes are discussed in section 5. Over North America and Europe,  $RE_{aci}$  causes a warming  
440 effect of up to  $+3 \text{ W/m}^2$ , driven solely by the effect on SW radiation (Fig. 3iii). Over the regions  
441 of East Asia and the Amazon and Congo basins,  $RE_{aci}$  reaches a maximum of  $+5 \text{ W/m}^2$ , driven by  
442 both the effect on the SW (up to  $+4 \text{ W/m}^2$ ) and LW (up to  $+1.5 \text{ W/m}^2$ ) parts of the radiation  
443 spectrum. The cooling effect of  $RE_{aci}$  (up to  $-2 \text{ W/m}^2$ ) extends mainly between the equatorial line  
444 and the Tropic of Cancer, mainly due to the interaction of nitrate aerosols with desert dust particles  
445 (e.g. from the Sahara) and their effect on the terrestrial spectrum (LW) (Figs. 1c & 3ii). The cooling  
446 effect of dust interactions with anthropogenic particles in the LW spectrum corroborates the  
447 findings of Klingmüller et al. (2020) and is attributed to the reduced ice-water path due to the  
448 depletion of small aerosols, which in turn leads to less trapped outgoing terrestrial radiation. In  
449 addition, Kok et al. (2023) note how the presence of dust particles leads to an optical thinning of  
450 cirrus clouds by reducing the number of ice crystals while increasing their size, which also leads  
451 to less trapping of outgoing LW radiation and thus a cooling effect (Fig. 1c). On the other hand,  
452 the warming effect of dust interactions with anthropogenic particles in the SW spectrum requires  
453 further investigation and is therefore discussed in more detail in Section 5.



454 **Figure 3:** Global mean TOA  $RE_{aci}$  for total  $\text{NO}_3^-$  aerosols. Estimates for (i) net, (ii) longwave, and (iii)  
455 shortwave, as calculated by EMAC from the base case simulation.



456 **Table 3:** Net, longwave, and shortwave global mean TOA  $RE_{aci}$  of total  $NO_3^-$  aerosols for the  
 457 base case and each sensitivity case simulations.

Simulation	TOA $RE_{aci}$ ( $W/m^2$ )		
	Net	LW	SW
Base Case	+ 0.17	- 0.10	+ 0.27
Chemically Inert Dust	+ 0.11	- 0.06	+ 0.17
Homogeneous Ion Composition	+ 0.13	- 0.09	+ 0.22
Half Dust Scenario	+ 0.15	- 0.08	+ 0.23
Increased Dust Scenario	+ 0.14	- 0.11	+ 0.25

458

459 **4.2 Sensitivity of  $RE_{aci}$  Estimates.**

460 Table 3 shows the comparison of the net, LW, and SW contributions of total  $NO_3^-$  to the  $RE_{aci}$   
 461 at the top of the atmosphere as calculated by the base case simulation and all sensitivity cases  
 462 considered. By assuming a chemically inert dust, the calculated net  $RE_{aci}$  of nitrate decreases by  
 463 35%, resulting in a net warming of +0.11  $W/m^2$ . As with the  $RE_{ari}$  estimate, this sensitivity case  
 464 produces the largest deviation from the base case among all sensitivity simulations, for both the  
 465 SW (37% less warming) and LW (40% less cooling) estimates. This is due to the fact that the  
 466 absence of dust-nitrate interactions does not have such a large impact on the population of both  
 467 aerosols and activated particles (see also Section 5). The assumption of a homogeneous ionic  
 468 composition of the mineral dust leads to a weakened LW cooling estimate of 10% and a weakened  
 469 SW warming estimate of 19% resulting in a net  $NO_3^-$   $RE_{aci}$  of +0.13  $W/m^2$  (24% lower than in the  
 470 base case).

471 The reduced dust emissions result in a 15% weaker warming in the SW spectrum and a 20%  
 472 weaker cooling in the LW spectrum, leading to an overall  $NO_3^-$   $RE_{aci}$  of +0.15  $W/m^2$  (12% weaker  
 473 than the base case scenario). This is because the reduced loading of nitrate aerosols, especially in  
 474 the coarse mode, in the half dust scenario results in less absorption of LW radiation (Fig. 1c) (hence  
 475 less cooling). Similarly, the effect of dust-nitrate interactions on the activation of smaller particles  
 476 (Fig. 1d) is less drastic and results in a weaker inhibition of SW radiation scattering (hence less  
 477 warming, see also Section 5). Finally, increased dust emissions in the increased dust scenario show  
 478 a 10% increase in the LW cooling and an 8% decrease in the SW warming effect, surprisingly  
 479 resulting in a net warming (+0.14  $W/m^2$ ) that is lower than in the half dust scenario. The reason  
 480 that this scenario results in more LW cooling than the base case is that the increased amount of  
 481 dust particles leads to even more optical thinning of the ice clouds, and therefore even less trapping  
 482 of LW radiation (more cooling). However, the reason why the SW warming estimate is lower than  
 483 the base case is more complicated. First, the transition from the half dust scenario to the base case  
 484 and then to the increased dust scenario does not lead to an analogous increase in the nitrate aerosol



485 burden (see Section 3.2). Moreover, since the number of aerosols has increased from the increased  
486 dust scenario to the base case, but the relative humidity has remained largely the same, there is  
487 more competition for water vapor because it is now distributed over a larger population. As a  
488 result, the wet radius increase in the presence of nitrates is not as strong in the increased dust  
489 scenario compared to the base case, and the depletion of smaller sized particles is also not as strong  
490 (not shown). The implications of the depletion of the aerosol population in the presence of nitrate  
491 aerosols on the microphysical processes of warm clouds, and consequently on SW warming, are  
492 discussed in the next section.

## 493 **5 Effect Of $\text{NO}_3^-$ Aerosols on Cloud Microphysics**

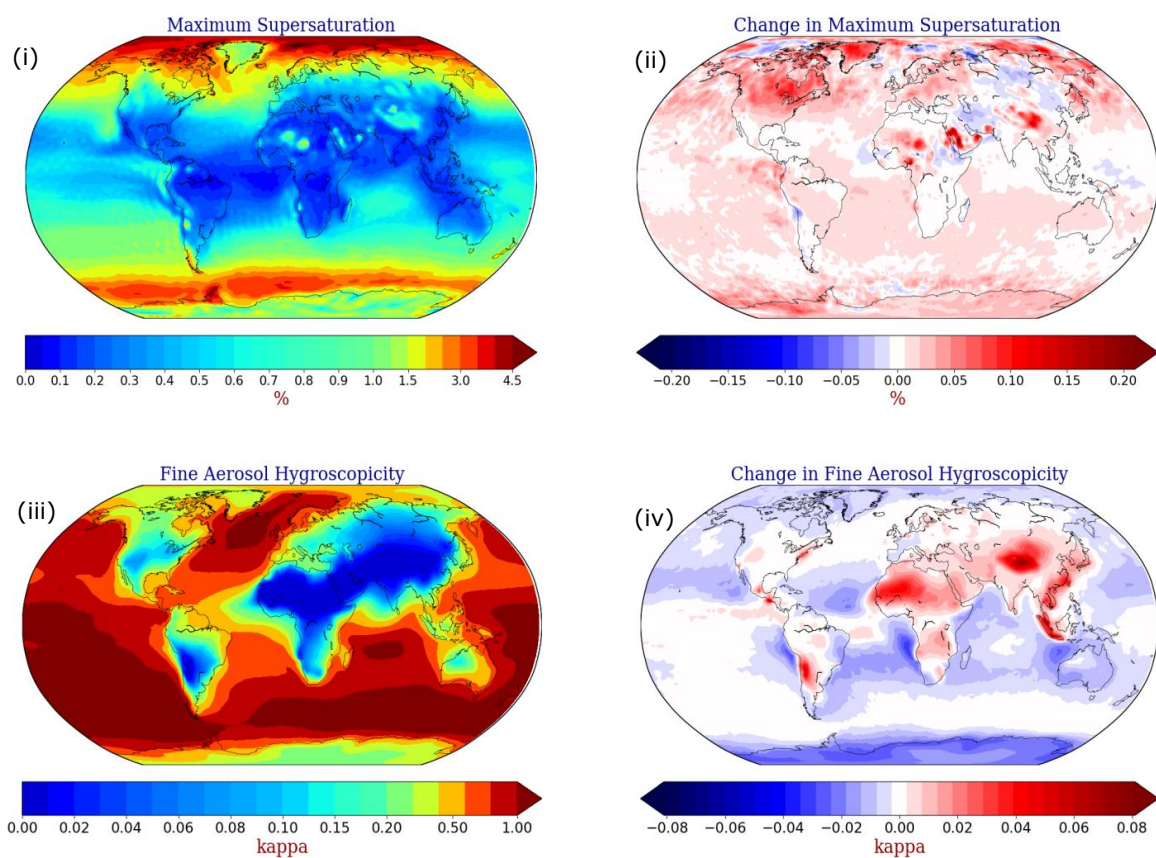
### 494 **5.1 Maximum Supersaturation, Hygroscopicity and Wet Radius**

495 To further investigate the cause of the positive  $\text{RE}_{\text{aci}}$  induced by the  $\text{NO}_3^-$  aerosols, their effect  
496 on the characteristics of the aerosol population as well as on the cloud microphysics is investigated,  
497 with respect to the lowest forming cloud level of 940 hPa. For this purpose, a sensitivity simulation  
498 is performed assuming a 'nitrate aerosol free' (NAF) atmosphere, in which the formation of  $\text{NO}_3^-$   
499 aerosols has been switched off, but an advanced cloud scheme is considered. This simulation is  
500 used to determine whether the presence of  $\text{NO}_3^-$  aerosols has a significant effect on the  
501 hygroscopicity and size of atmospheric aerosols and ultimately on the maximum supersaturation  
502 developed during cloud formation. Over polluted areas affected by transported dust air masses  
503 from surrounding arid areas, the presence of  $\text{NO}_3^-$  aerosols can increase the CCN activity of the  
504 large mineral dust particles, resulting in a reduction of the maximum supersaturation and inhibiting  
505 the activation of the small anthropogenic particles into cloud droplets (Klingmüller et al., 2020).  
506 Results from the NAF sensitivity simulation support this hypothesis over parts of Eastern and  
507 Central Asia, where the maximum supersaturation decreases by up to 0.05%. In contrast, the  
508 presence of  $\text{NO}_3^-$  aerosols increases maximum supersaturation by up to 0.2% over North America,  
509 Europe, the Middle East, and parts of southern Asia (Fig. 4ii). Therefore, changes in maximum  
510 supersaturation caused by the presence of  $\text{NO}_3^-$  aerosols cannot explain their warming effect  
511 through the  $\text{RE}_{\text{aci}}$ .

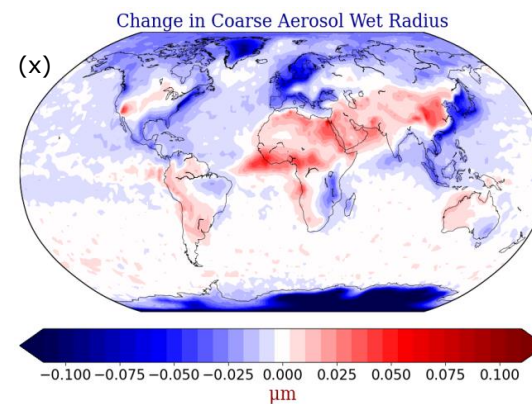
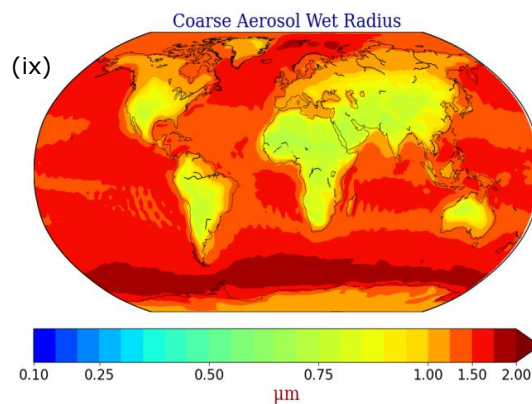
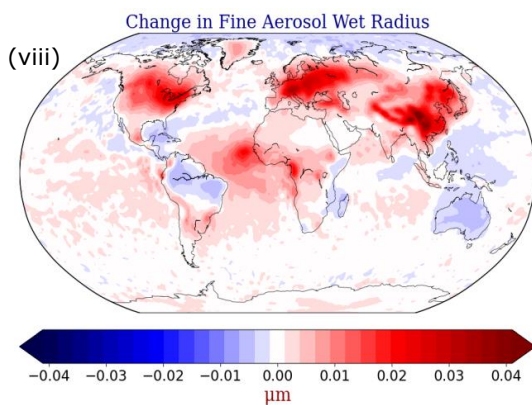
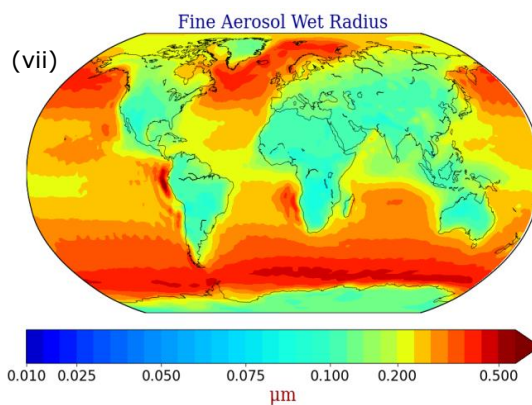
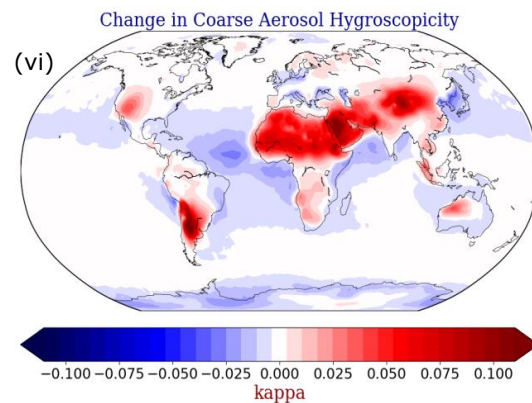
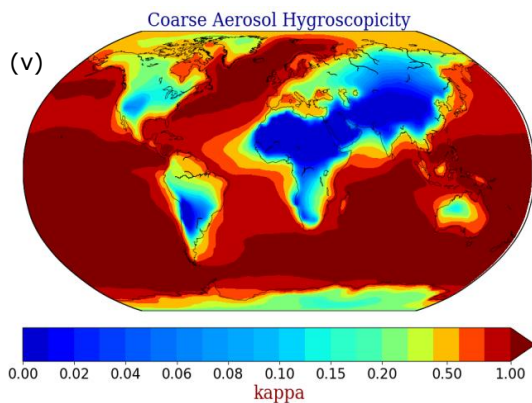
512 The presence of  $\text{NO}_3^-$  has a significant effect on the hygroscopicity of both fine and coarse  
513 aerosols and consequently on their wet radius, as shown in Figures 1a, b & 4. This is most evident  
514 for coarse desert dust particles, which mix with  $\text{NO}_3^-$  aerosols from urban and forest regions,  
515 increasing their hygroscopicity by an order of magnitude (up to 0.1), especially over the African-  
516 Asian dust belt and the Atacama Desert in South America (Fig. 4vi). Aerosol hygroscopicity is  
517 similarly increased for the fine mode particles both near arid regions and over the highly  
518 industrialized region of Southeast Asia (Fig. 4iv). On the other hand, the aerosol hygroscopicity  
519 for the two size modes is only slightly reduced, by up to 0.06 (or <10%) over the oceans and coasts  
520 of Europe and East Asia, due to interactions of  $\text{NO}_3^-$  with sea salt particles, reducing their  
521 hygroscopicity. The increased ability of both coarse dust aerosols and smaller aerosols to absorb  
522 water leads to an increase in their wet radius, but in different parts of the world. For example, fine  
523 particle sizes increase by up to 0.04  $\mu\text{m}$  (up to 40%) mostly over regions of high anthropogenic  
524 activity (North America, Europe, and East Asia) (Fig. 4viii). On the other hand, coarse mode  
525 particle sizes are increased by up to 0.1  $\mu\text{m}$  (up to 10%) over the forests of central Africa and the



526 African-Asian dust belt zone (Fig. 4x), while showing a similar decrease near the coasts of the  
527 polluted northern hemisphere due to the effect of  $\text{NO}_3^-$  on the hygroscopicity of sea salt.  
528









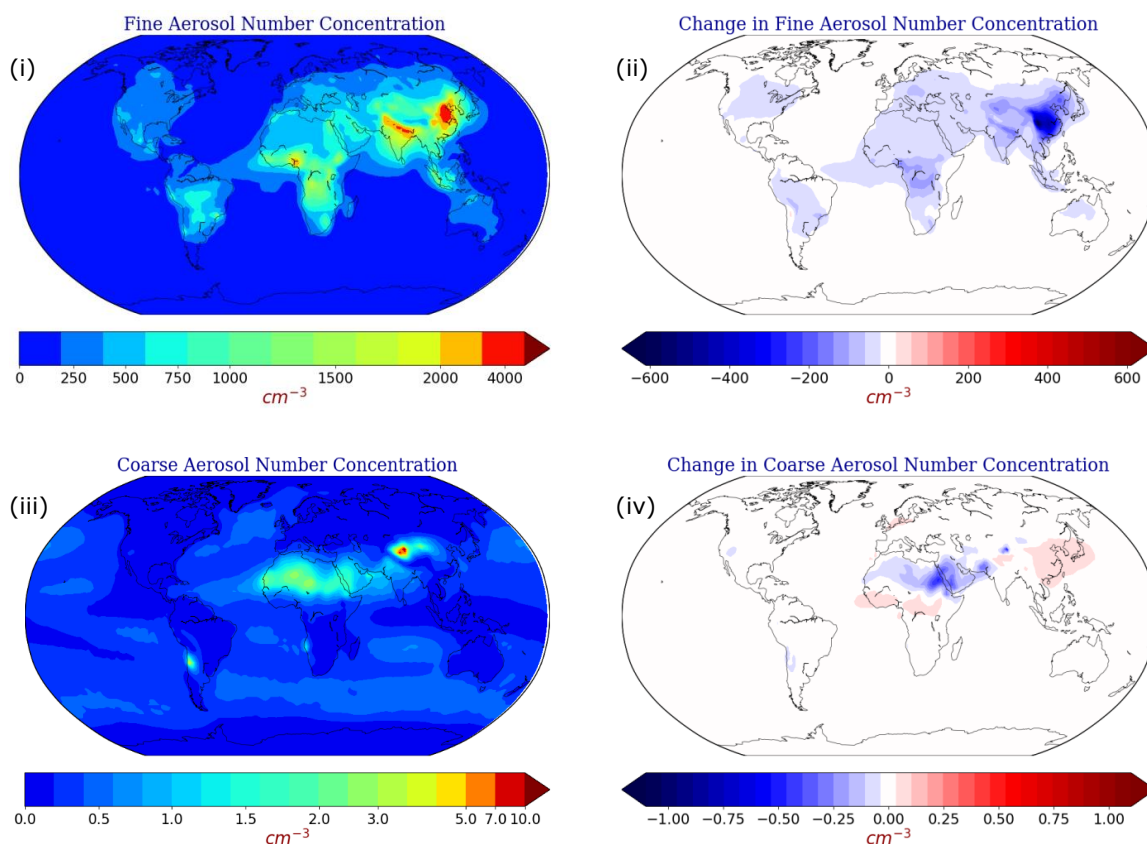
530 **Figure 4:** (i) Global mean maximum supersaturation, fine aerosol (iii) hygroscopicity and (v) wet  
531 radius, and coarse aerosol (vii) hygroscopicity and (ix) wet radius, as calculated by EMAC from  
532 the base case simulation at the altitude of 940 hPa. Absolute difference between base case and  
533 Nitrate Aerosol Free (NAF) sensitivity simulation in (ii) maximum supersaturation, fine aerosol  
534 (iv) hygroscopicity and (vi) wet radius, and coarse aerosol (viii) hygroscopicity and (x) wet radius  
535 at the altitude of 940 hPa. Red indicates higher values calculated by the base case simulation in  
536 the presence of  $\text{NO}_3^-$  aerosols.

## 537 **5.2 Number Concentrations of Aerosol and Activated Particles.**

538 Figure 5 shows the effect of  $\text{NO}_3^-$  on the number concentration of fine and coarse aerosols  
539 between the base case and the 'NAF' sensitivity simulation, as well as the total aerosol population.  
540 The presence of  $\text{NO}_3^-$  aerosols decreases the total aerosol number concentration over forests and  
541 polluted regions (see also Fig. 1d). This behavior is driven solely by the decrease in smaller particle  
542 sizes, as the effect is minimal for the coarser particles (Figs. 5ii & 5iv). The largest decrease is  
543 calculated over East and South Asia (up to  $1000 \text{ cm}^{-3}$  or 10%), while decreases of up to  $200 \text{ cm}^{-3}$   
544 on average ( $\sim 10\%$ ) are found over Europe, the USA, and Central Africa. This effect is directly  
545 related to the increased wet radius of the aerosol population (Fig. 4viii) over these regions and thus  
546 to its depositional efficiency. In addition, coarse dust particles become more hygroscopic due to  
547 interactions with  $\text{NO}_3^-$  aerosols that increase in size, resulting in increased coagulation with the  
548 smaller anthropogenic particles, which reduces their abundance.

549 The reduced aerosol number concentration in the presence of  $\text{NO}_3^-$  can lead to a reduction of  
550 particles that are also activated into cloud droplets. Such behavior can be seen in Figure 6, which  
551 shows the effect of  $\text{NO}_3^-$  on the number concentration of activated fine and coarse particles in  
552 cloud droplets between the base case and the 'NAF' sensitivity simulation. The reduction in the  
553 total number of activated cloud droplets is almost entirely due to the reduction in smaller size  
554 particles (Figs. 6ii & 6iv). A reduction in the total number of activated droplets of up to  $30 \text{ cm}^{-3}$  or  
555 10% is observed over the USA, Amazon, Europe, Central Africa, and parts of the Middle East,  
556 while this reduction reaches up to  $100 \text{ cm}^{-3}$  (10%) over Southeast Asia, where the largest reductions  
557 in aerosol numbers are also calculated (Fig. 4ii). In turn, these are the regions where the warming  
558 effect of  $\text{NO}_3^-$  aerosols on the calculated mean  $\text{RE}_{\text{aci}}$  is strongest (Figure 3i). The small increase in  
559 activated droplets ( $\sim 10 \text{ cm}^{-3}$  or 1%) over Beijing, which concerns the fine mode particles, is most  
560 likely because their number concentration decreases with increasing size. The high aerosol number  
561 concentration there, which is the global maximum (Figure 5i), results in a hotspot of more readily  
562 activated particles in the presence of  $\text{NO}_3^-$ . On the other hand, the CDNC decreases slightly over  
563 the Sahara due to the more efficient deposition capacity of coarse dust particles due to their  
564 interactions with nitrate aerosols, which is also reflected in the decrease in aerosol number (Fig.  
565 6iv). Overall, the lower particle number in the presence of  $\text{NO}_3^-$  aerosols hinders the ability of the  
566 smaller anthropogenic particles to activate into cloud droplets, leading to a reduced cloud cover  
567 and thus a reduced cloud albedo effect. Therefore, not only less LW radiation is absorbed, but  
568 more importantly, less SW radiation is scattered back to space, resulting in an overall warming of  
569 the net average  $\text{RE}_{\text{aci}}$  for total  $\text{NO}_3^-$  aerosols.

570



571

572 **Figure 5:** Global mean number concentration of (i) fine and (iii) coarse aerosols as calculated by EMAC  
573 from the base case simulation at the altitude of 940 hPa. Absolute difference between the base case and the  
574 Nitrate Aerosol Free (NAF) sensitivity simulation in the number concentration of (ii) fine and (iv) coarse  
575 aerosols at the altitude of 940 hPa. Blue indicates that number concentrations are lower in the presence of  
576  $\text{NO}_3^-$  aerosols.

577

578

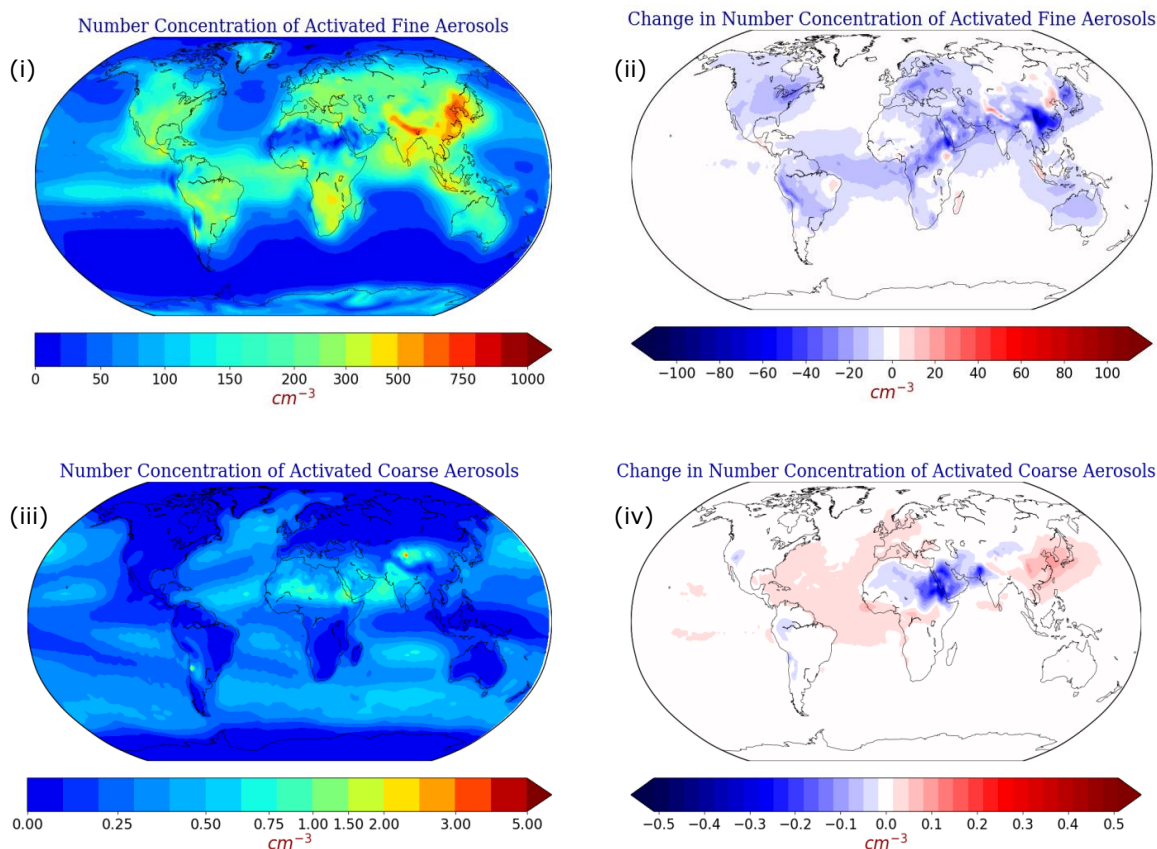
579

580

581

582

583



584

585 **Figure 6:** Global mean number concentration of activated (i) fine and (iii) coarse aerosols as calculated by  
 586 EMAC from the base case simulation at the altitude of 940 hPa. Absolute difference between the base case  
 587 and the Nitrate Aerosol Free (NAF) sensitivity simulation in the number concentration of activated (ii) fine  
 588 and (iv) coarse aerosols at the altitude of 940 hPa. Blue indicates that number concentrations are lower in  
 589 the presence of  $\text{NO}_3^-$  aerosols.

590

## 591 6. Conclusions and Discussion

592 This study presents the effects of interactions between mineral dust and  $\text{NO}_3^-$  aerosols on the  
 593 present-day global TOA radiative effect of the latter. We investigate how the presence of dust  
 594 affects the radiative effect of  $\text{NO}_3^-$  aerosols, both through aerosol interactions with radiation and  
 595 separately with clouds ( $\text{RE}_{\text{ari}}$  and  $\text{RE}_{\text{aci}}$ , respectively). Sensitivity simulations are also performed,  
 596 varying both the mineral dust composition and its emissions, to assess their effect on the calculated  
 597  $\text{NO}_3^-$  aerosol radiative effect.

598 It was found that the global average net  $\text{RE}_{\text{ari}}$  of total  $\text{NO}_3^-$  aerosols is  $-0.11 \text{ W/m}^2$ , which is  
 599 mainly due to the cooling from the shortwave part of the radiation spectrum due to scattering,





600 equal to  $-0.34 \text{ W/m}^2$ . A warming from the longwave part of the spectrum due to absorption was  
601 found to be  $+0.23 \text{ W/m}^2$  on global average and was mainly located over regions with high  
602 concentrations of coarse  $\text{NO}_3^-$  aerosols. SW cooling was also observed in these regions, but also  
603 over regions of high anthropogenic activity, mainly over the polluted northern hemisphere. The  
604 overall sign of the net  $\text{RE}_{\text{ari}}$  for total  $\text{NO}_3^-$  aerosols was dominated by the behavior of the coarse  
605 mode particles, which contributed on average  $-0.09 \text{ W/m}^2$ . Specifically, coarse nitrate particles  
606 were responsible for 82% of the net cooling and 100% of the net warming, while the fine mode  
607 played a minor role. The sensitivity experiments revealed that the chemistry of the mineral dust is  
608 the most important factor in changing the estimated  $\text{RE}_{\text{ari}}$  of the total  $\text{NO}_3^-$  aerosols. In particular,  
609 LW warming is most affected by this assumption, being 52% weaker after assuming chemically  
610 inert dust emissions, while the SW cooling is reduced by 41% compared to the base case  
611 simulation, amounting to a net cooling of  $-0.09 \text{ W/m}^2$ . A globally homogeneous ionic composition  
612 for mineral dust had a smaller effect in LW (22% decrease) and SW (21% decrease) but resulted  
613 in the same net estimate of  $-0.09 \text{ W/m}^2$ . Halving the dust emissions resulted in weaker estimates  
614 for LW and SW by 17% and 21%, respectively, and the lowest overall net  $\text{RE}_{\text{ari}}$  of  $-0.08 \text{ W/m}^2$ .  
615 On the other hand, a 50% increase in dust emissions increased both LW warming and SW cooling  
616 by 17% and 9% respectively, resulting in a net cooling  $\text{RE}_{\text{ari}}$  of  $-0.10 \text{ W/m}^2$ , indicating the strong  
617 non-linear relationship of nitrate-dust interactions and how they affect the radiative effect  
618 estimates.

619 The global average net  $\text{RE}_{\text{aci}}$  of total  $\text{NO}_3^-$  aerosols was  $+0.17 \text{ W/m}^2$  due to the effect on the  
620 shortwave portion of the spectrum. This was found to be  $+0.27 \text{ W/m}^2$ , while the cooling from the  
621 longwave part was  $-0.10 \text{ W/m}^2$ . Spatially, the net  $\text{RE}_{\text{aci}}$  is reversed compared to the net  $\text{RE}_{\text{ari}}$  for  
622 total  $\text{NO}_3^-$  aerosols, where regions responsible for a strong SW cooling of the  $\text{RE}_{\text{ari}}$  contribute to a  
623 strong SW warming of the  $\text{RE}_{\text{aci}}$  and vice versa. This is due to the fact that nitrate-dust interactions  
624 challenge the dominance of smaller particles over heavily polluted regions, reducing the  
625 reflectivity of warm cloud and thus having an opposite effect on the  $\text{RE}_{\text{aci}}$ . The sensitivity  
626 experiments again showed that the consideration of the chemistry of the mineral dust is important  
627 for the calculation of the  $\text{RE}_{\text{aci}}$  of the total  $\text{NO}_3^-$  aerosols. When the dust was assumed to be  
628 chemically inert, the LW and SW estimates were up to 40% weaker, resulting in a warming of  
629  $+0.11 \text{ W/m}^2$ . Assuming a homogeneous ion composition resulted in a smaller weakening of the  
630 estimates (up to 18%) and a net warming of  $+0.13 \text{ W/m}^2$ . When dust emissions were halved, the  
631 LW cooling was reduced slightly more than in the base case, resulting in a net warming of  $+0.15$   
632  $\text{W/m}^2$ . The 50% increase in dust emissions had the largest effect on LW behavior (10% increase),  
633 but surprisingly the net estimate ( $+0.14 \text{ W/m}^2$ ) was smaller than in the half-dust scenario. The  
634 reason for this is that the SW estimate did not increase but decreased by 8% due to the fact that in  
635 this scenario the increased nitrate burden causes increased competition for the available  
636 supersaturation and the effect of dust-nitrate interactions on the smaller aerosol populations is not  
637 as emphasized as in the base case.

638 The total  $\text{NO}_3^-$  aerosol  $\text{RE}_{\text{aci}}$  shows a positive sign, which is attributed to a reduced cloud albedo  
639 effect. More specifically, although the presence or absence of  $\text{NO}_3^-$  aerosol in the atmosphere did  
640 not significantly affect the total available maximum supersaturation, it did alter both the  
641 hygroscopicity and wet radii of the aerosols. In the presence of  $\text{NO}_3^-$ , the hygroscopicity of aerosols  
642 over deserts was increased by up to an order of magnitude, leading to an increase in their wet





643 radius of up to 10%, with an even larger increase of up to 40% for smaller particles over urban  
644 regions. Therefore, in the presence of  $\text{NO}_3^-$  aerosols, there is an increased depletion of fine particles  
645 by coagulation with coarser particles (i.e. mineral dust) that have been further increased in size.  
646 The reduction in the number of aerosols is as much as 10% in some regions, with maximum  
647 reductions calculated over Southeast Asia. This reduction in the number of fine aerosols leads to  
648 a reduction in the number of cloud droplets activated by fine aerosols (also up to 10%), which  
649 would otherwise have absorbed more outgoing longwave radiation and, more importantly,  
650 scattered more incoming shortwave radiation. Thus, the reduced cloud albedo effect leads to a  
651 cooling in the longwave part of the spectrum, which is offset by a strong warming in the shortwave  
652 part.  
653



#### 654 **Code and Data Availability**

655 The usage of MESSy (Modular Earth Submodel System) and access to the source code is licensed  
656 to all affiliates of institutions which are members of the MESSy Consortium. Institutions can  
657 become a member of the MESSy Consortium by signing the “MESSy Memorandum of  
658 Understanding”. More information can be found on the MESSy Consortium website:  
659 <http://www.messy-interface.org> (last access: 22 May 2024). The code used in this study has been  
660 based on MESSy version 2.55 and is archived with a restricted access DOI  
661 (<https://doi.org/10.5281/zenodo.8379120>, The MESSy Consortium, 2023). The data produced in  
662 the study is available from the authors upon request.

663

#### 664 **Acknowledgements**

665 This work was supported by the project FORCeS funded from the European Union’s Horizon 2020  
666 research and innovation program under grant agreement No 821205. JFK was funded by the  
667 National Science Foundation (NSF) Directorate for Geosciences grants 1856389 and 2151093.  
668 The work described in this paper has received funding from the Initiative and Networking Fund of  
669 the Helmholtz Association through the project “Advanced Earth System Modelling Capacity  
670 (ESM)”. The authors gratefully acknowledge the Earth System Modelling Project (ESM) for  
671 funding this work by providing computing time on the ESM partition of the supercomputer  
672 JUWELS (Alvarez, 2021) at the Jülich Supercomputing Centre (JSC).

673

#### 674 **Competing Interests**

675 At least one of the (co-)authors is a member of the editorial board of Atmospheric Chemistry and  
676 Physics.

#### 677 **Author Contributions**

678 AM and VAK wrote the paper with contributions from KK, APT, JFK, MK, and AN. VAK  
679 planned the research with contributions from APT, MK and AN. AM, KK and VAK designed the  
680 methodology for the radiative effect calculations. AM performed the simulations and analyzed the  
681 results, assisted by VAK and APT. All the authors discussed the results and contributed to the  
682 paper.

683

684



## 685 REFERENCES

- 686 Albrecht, B. A.: Aerosols, Cloud Microphysics, and Fractional Cloudiness, *Science*, 245(4923), 1227-1230,  
687 <https://doi.org/10.1126/science.245.4923.1227> , 1989.
- 688 Alvarez, D.: JUWELS cluster and booster: Exascale pathfinder with modular supercomputing architecture  
689 at juelich supercomputing Centre. *Journal of large-scale research facilities JLSRF*, 7, A183-A183,  
690 <https://doi.org/10.17815/jlsrf-7-183>, 2021.
- 691 Arias, P.A., N. Bellouin, E. Coppola, R.G. Jones, G. Krinner, J. Marotzke, V. Naik, M.D. Palmer, G.-K.  
692 Plattner, J. Rogelj, M. Rojas, J. Sillmann, T. Storelvmo, P.W. Thorne, B. Trewin, K. Achuta Rao, B.  
693 Adhikary, R.P. Allan, K. Armour, G. Bala, R. Barimalala, S. Berger, J.G. Canadell, C. Cassou, A. Cherchi,  
694 W. Collins, W.D. Collins, S.L. Connors, S. Corti, F. Cruz, F.J. Dentener, C. Dereczynski, A. Di Luca, A.  
695 Diongue Niang, F.J. Doblas-Reyes, A. Dosio, H. Douville, F. Engelbrecht, V. Eyring, E. Fischer, P.  
696 Forster, B. Fox-Kemper, J.S. Fuglestad, J.C. Fyfe, N.P. Gillett, L. Goldfarb, I. Gorodetskaya, J.M.  
697 Gutierrez, R. Hamdi, E. Hawkins, H.T. Hewitt, P. Hope, A.S. Islam, C. Jones, D.S. Kaufman, R.E. Kopp, Y.  
698 Kosaka, J. Kossin, S. Krakovska, J.-Y. Lee, J. Li, T. Mauritsen, T.K. Maycock, M. Meinshausen, S.-K. Min,  
699 P.M.S. Monteiro, T. Ngo-Duc, F. Otto, I. Pinto, A. Pirani, K. Raghavan, R. Ranasinghe, A.C. Ruane, L.  
700 Ruiz, J.-B. Sallée, B.H. Samset, S. Sathyendranath, S.I. Seneviratne, A.A. Sörensson, S. Szopa, I.  
701 Takayabu, A.-M. Tréguier, B. van den Hurk, R. Vautard, K. von Schuckmann, S. Zaehle, X. Zhang, and  
702 K. Zickfeld, 2021: Technical Summary. In *Climate Change 2021: The Physical Science Basis. Contribution of Working Group I to the Sixth Assessment Report of the Intergovernmental Panel on Climate Change* [Masson-Delmotte, V., P. Zhai, A. Pirani, S.L. Connors, C. Péan, S. Berger, N. Caud, Y. Chen, L. Goldfarb, M.I. Gomis, M. Huang, K. Leitzell, E. Lonnoy, J.B.R. Matthews, T.K. Maycock, T. Waterfield, O. Yelekçi, R. Yu, and B. Zhou (eds.)]. Cambridge University Press, Cambridge, United Kingdom and New York, NY, USA, <https://doi.org/10.1017/9781009157896.002> , 2021.
- 708 Astitha, M., Lelieveld, J., Kader, M. A., Pozzer, A., and de Meij, A.: Parameterization of dust emissions in  
709 the global atmospheric chemistry-climate model EMAC: impact of nudging and soil properties,  
710 *Atmospheric Chemistry and Physics* , 12(22), 11057-11083, [https://doi.org/10.5194/acp-12-11057-](https://doi.org/10.5194/acp-12-11057-2012)  
711 [2012](https://doi.org/10.5194/acp-12-11057-2012) , 2012.
- 712 Bacer, S., Sullivan, S. C., Karydis, V. A., Barahona, D., Kramer, M., Nenes, A., Tost, H., Tsimpidi, A. P.,  
713 Lelieveld, J., and Pozzer, A.: Implementation of a comprehensive ice crystal formation  
714 parameterization for cirrus and mixed-phase clouds in the EMAC model (based on MESSy 2.53),  
715 *Geoscientific Model Development* , 11(10), <https://doi.org/10.5194/gmd-11-4021-2018> , 2018.
- 716 Barahona, D. and Nenes, A.: Parameterizing the competition between homogeneous and heterogeneous  
717 freezing in cirrus cloud formation - monodisperse ice nuclei, *Atmospheric Chemistry and Physics* ,  
718 9(16), 369-381, <https://doi.org/10.5194/acp-9-5933-2009> , 2009.
- 719 Barahona, D., West, R., Stier, P., Romakkaniemi, S., Kokkola, H., and Nenes, A.: Comprehensively  
720 accounting for the effect of giant CCN in cloud activation parameterizations, *Atmospheric Chemistry*  
721 *and Physics* , 10(5) , 2467-2473, <https://doi.org/10.5194/acp-10-2467-2010> , 2010.
- 722 Bauer, S. E., Koch, D., Unger, N., Metzger, S. M., Shindell, D. T., and Streets, D. G.: Nitrate aerosols today  
723 and in 2030: a global simulation including aerosols and tropospheric ozone, *Atmospheric Chemistry*  
724 *and Physics* , 7(19) , <https://doi.org/10.5194/acp-7-5043-2007> , 2007a.
- 725 Bauer, S. E., Mishchenko, M. I., Lacis, A. A., Zhang, S., Perlwitz, J., and Metzger, S. M.: Do sulfate and  
726 nitrate coatings on mineral dust have important effects on radiative properties and climate  
727 modeling?, *Journal of Geophysical Research: Atmospheres*, 112(D6),  
728 <https://doi.org/10.1029/2005JD006977> , 2007b.
- 729 Bellouin, N., Rae, J., Jones, A., Johnson, C., Haywood, J., and Boucher, O.: Aerosol forcing in the Climate  
730 Model Intercomparison Project (CMIP5) simulations by HadGEM2-ES and the role of ammonium



- 731 nitrate, *Journal of Geophysical Research: Atmospheres*, 116(D20) ,  
732 <https://doi.org/10.1029/2011JD016074> , 2011.
- 733 Bond, T. C. and Bergstrom, R. W.: Light absorption by carbonaceous particles: An investigative review,  
734 *Aerosol Science and Technology*, 40(1), 27-67, <https://doi.org/10.1080/02786820500421521> , 2006.
- 735 Bouwman, A. F., Lee, D. S., Asman, W. A. H., Dentener, F. J., VanderHoek, K. W., and Olivier, J. G. J.: A  
736 global high-resolution emission inventory for ammonia, *Global Biogeochemical Cycles* , 11(4) ,  
737 <https://doi.org/10.1029/97GB02266> , 1997.
- 738 Dentener, F., Kinne, S., Bond, T., Boucher, O., Cofala, J., Generoso, S., Ginoux, P., Gong, S., Hoelzemann,  
739 J. J., Ito, A., Marelli, L., Penner, J. E., Putaud, J. P., Textor, C., Schulz, M., van der Werf, G. R., and  
740 Wilson, J.: Emissions of primary aerosol and precursor gases in the years 2000 and 1750 prescribed  
741 data-sets for AeroCom, *Atmospheric Chemistry and Physics* , 6(12) , 4321-4344,  
742 <https://doi.org/10.5194/acp-6-4321-2006> , 2006.
- 743 Di Biagio, C., Formenti, P., Balkanski, Y., Caponi, L., Cazaunau, M., Pangu, E., Journet, E., Nowak, S.,  
744 Andreae, M. O., Kandler, K., Saeed, T., Piketh, S., Seibert, D., Williams, E., and Doussin, J. F.: Complex  
745 refractive indices and single-scattering albedo of global dust aerosols in the shortwave spectrum and  
746 relationship to size and iron content, *Atmospheric Chemistry and Phys.*, 19(24), 15503-15531,  
747 <https://doi.org/10.5194/acp-19-15503-2019> , 2019.
- 748 Dietmuller, S., Jockel, P., Tost, H., Kunze, M., Gellhorn, C., Brinkop, S., Fromming, C., Ponater, M., Steil,  
749 B., Lauer, A., and Hendricks, J.: A new radiation infrastructure for the Modular Earth Submodel  
750 System (MESSy, based on version 2.51), *Geoscientific Model Development*, 9(6) , 2209-2222,  
751 <https://doi.org/10.5194/gmd-9-2209-2016> , 2016.
- 752 Fan, S.-M., Horowitz, L. W., Levy, H., and Moxim, W. J.: Impact of air pollution on wet deposition of  
753 mineral dust aerosols, *Geophysical Research Letters*, 31(2), <https://doi.org/10.1029/2003GL018501> ,  
754 2004.
- 755 Fountoukis, C. and Nenes, A.: ISORROPIA II: a computationally efficient thermodynamic equilibrium model  
756 for  $K^+$ - $Ca^{2+}$ - $Mg^{2+}$ - $NH_4^+$ - $Na^+$ - $SO_4^{2-}$ - $NO_3^-$ - $Cl^-$ - $H_2O$  aerosols, *Atmospheric Chemistry and Physics*, 7, 4639-  
757 4659, 2007.
- 758 Fuchs, N. A. and Davies, C. N.: *The mechanics of aerosols*, Pergamon Press, Oxford, ISBN  
759 9780486660554, 1964.
- 760 Gao, M., Ji, D., Liang, F., and Liu, Y.: Attribution of aerosol direct radiative forcing in China and India to  
761 emitting sectors, *Atmospheric Environment*, 190, 35-42,  
762 <https://doi.org/10.1016/j.atmosenv.2018.07.011> , 2018.
- 763 Ghan, S. J., Liu, X., Easter, R. C., Zaveri, R., Rasch, P. J., Yoon, J. H., and Eaton, B.: Toward a Minimal  
764 Representation of Aerosols in Climate Models: Comparative Decomposition of Aerosol Direct,  
765 Semidirect, and Indirect Radiative Forcing, *Journal of Climate*, 25(19), 6461-6476,  
766 <https://doi.org/10.1175/JCLI-D-11-00650.1> , 2012.
- 767 Grewe, V., Brunner, D., Dameris, M., Grenfell, J. L., Hein, R., Shindell, D., and Staehelin, J.: Origin and  
768 variability of upper tropospheric nitrogen oxides and ozone at northern mid-latitudes, *Atmospheric  
769 Environment*, 35(20), 3421-3433, [https://doi.org/10.1016/S1352-2310\(01\)00134-0](https://doi.org/10.1016/S1352-2310(01)00134-0) , 2001.
- 770 Hauglustaine, D. A., Balkanski, Y., and Schulz, M.: A global model simulation of present and future nitrate  
771 aerosols and their direct radiative forcing of climate, *Atmospheric Chemistry and Physics*, 14(20),  
772 11031-11063, <https://doi.org/10.5194/acp-14-11031-2014> , 2014.
- 773 IPCC, 2013: *Climate Change 2013: The Physical Science Basis*. Contribution of Working Group I to the  
774 Fifth Assessment Report of the Intergovernmental Panel on Climate Change [Stocker, T.F., D. Qin, G.-  
775 K. Plattner, M. Tignor, S.K. Allen, J. Boschung, A. Nauels, Y. Xia, V. Bex and P.M. Midgley (eds.)].  
776 Cambridge University Press, Cambridge, United Kingdom and New York, NY, USA.



- 777 Jockel, P., Sander, R., Kerkweg, A., Tost, H., and Lelieveld, J.: Technical note: The Modular Earth  
778 Submodel System (MESSy) - a new approach towards Earth System Modeling, *Atmos Chem Phys*,  
779 5(2), 433-444, <https://doi.org/10.5194/acp-5-433-2005> , 2005.
- 780 Jockel, P., Tost, H., Pozzer, A., Bruhl, C., Buchholz, J., Ganzeveld, L., Hoor, P., Kerkweg, A., Lawrence, M.  
781 G., Sander, R., Steil, B., Stiller, G., Tanarhte, M., Taraborrelli, D., Van Aardenne, J., and Lelieveld, J.:  
782 The atmospheric chemistry general circulation model ECHAM5/MESSy1: consistent simulation of  
783 ozone from the surface to the mesosphere, *Atmospheric Chemistry and Physics*, 6(12), 5067-5104,  
784 <https://doi.org/10.5194/acp-6-5067-2006> , 2006.
- 785 Kakavas, S., Pandis, S. N., and Nenes, A.: ISORROPIA-Lite: A Comprehensive Atmospheric Aerosol  
786 Thermodynamics Module for Earth System Models, *Tellus Series B-Chemical and Physical*  
787 *Meteorology*, 74(1), 1-23, <https://doi.org/10.16993/tellusb.33> , 2022.
- 788 Kanakidou, M., Seinfeld, J. H., Pandis, S. N., Barnes, I., Dentener, F. J., Facchini, M. C., Van Dingenen, R.,  
789 Ervens, B., Nenes, A., Nielsen, C. J., Swietlicki, E., Putaud, J. P., Balkanski, Y., Fuzzi, S., Horth, J.,  
790 Moortgat, G. K., Winterhalter, R., Myhre, C. E. L., Tsigaridis, K., Vignati, E., Stephanou, E. G., and  
791 Wilson, J.: Organic aerosol and global climate modelling: a review, *Atmospheric Chemistry and*  
792 *Physics*, 5(4), 1053-1123, <https://doi.org/10.5194/acp-5-1053-2005> , 2005.
- 793 Karydis, V. A., Kumar, P., Barahona, D., Sokolik, I. N., and Nenes, A.: On the effect of dust particles on  
794 global cloud condensation nuclei and cloud droplet number, *Journal of Geophysical Research:*  
795 *Atmospheres*, 116, <https://doi.org/10.1029/2011JD016283>, 2011.
- 796 Karydis, V. A., Tsimpidi, A. P., Pozzer, A., Astitha, M., and Lelieveld, J.: Effects of mineral dust on global  
797 atmospheric nitrate concentrations, *Atmospheric Chemistry and Physics*, 16(3), 1491-1509,  
798 <https://doi.org/10.5194/acp-16-1491-2016> , 2016.
- 799 Karydis, V. A., Tsimpidi, A. P., Bacer, S., Pozzer, A., Nenes, A., and Lelieveld, J.: Global impact of mineral  
800 dust on cloud droplet number concentration, *Atmospheric Chemistry and Physics*, 17(9), 5601-5621,  
801 <https://doi.org/10.5194/acp-17-5601-2017> , 2017.
- 802 Kelly, J. T., Chuang, C. C., and Wexler, A. S.: Influence of dust composition on cloud droplet formation,  
803 *Atmospheric Environment*, 41(14), 2904-2916, <https://doi.org/10.1016/j.atmosenv.2006.12.008> ,  
804 2007.
- 805 Kerkweg, A., Buchholz, J., Ganzeveld, L., Pozzer, A., Tost, H., and Jockel, P.: Technical note: An  
806 implementation of the dry removal processes DRY DEPosition and SEDimentation in the modular  
807 earth submodel system (MESSy), *Atmospheric Chemistry and Physics*, 6(12), 4617-4632,  
808 <https://doi.org/10.5194/acp-6-4617-2006> , 2006.
- 809 Khain, A. P. and Pinsky, M.: *Physical Processes in Clouds and Cloud Modeling*, Cambridge University  
810 Press, ISBN 9781139049481, 2018.
- 811 Kirchstetter, T. W., Novakov, T., and Hobbs, P. V.: Evidence that the spectral dependence of light  
812 absorption by aerosols is affected by organic carbon, *Journal of Geophysical Research: Atmospheres*,  
813 109(D21), <https://doi.org/10.1029/2004JD004999> , 2004.
- 814 Klingmüller, K., Metzger, S., Abdelkader, M., Karydis, V. A., Stenchikov, G. L., Pozzer, A., and Lelieveld, J.:  
815 Revised mineral dust emissions in the atmospheric chemistry-climate model EMAC (MESSy 2.52  
816 DU\_Astitha1 KKDU2017 patch), *Geoscientific Model Development*, 11(3), 989-1008,  
817 <https://doi.org/10.5194/gmd-11-989-2018> , 2018.
- 818 Klingmüller, K., Lelieveld, J., Karydis, V. A., and Stenchikov, G. L.: Direct radiative effect of dust-pollution  
819 interactions, *Atmospheric Chemistry and Physics*, 19(11), 7397-7408, <https://doi.org/10.5194/acp-19-7397-2019> , 2019.
- 820  
821 Klingmüller, K., Karydis, V. A., Bacer, S., Stenchikov, G. L., and Lelieveld, J.: Weaker cooling by aerosols  
822 due to dust-pollution interactions, *Atmospheric Chemistry and Physics*, 20(23), 15285-15295,  
823 <https://doi.org/10.5194/acp-20-15285-2020> , 2020.





- 824 Kok, J. F., Storelvmo, T., Karydis, V. A., Adebisi, A. A., Mahowald, N. M., Evan, A. T., He, C., and Leung, D.  
825 M.: Mineral dust aerosol impacts on global climate and climate change, *Nature Reviews Earth &*  
826 *Environment*, 4(2), 71-86, <https://doi.org/10.1038/s43017-022-00379-5> , 2023.
- 827 Lance, S., Nenes, A., and Rissman, T. A.: Chemical and dynamical effects on cloud droplet number:  
828 Implications for estimates of the aerosol indirect effect, *Journal of Geophysical Research:*  
829 *Atmospheres*, 109(D22), <https://doi.org/10.1029/2004JD004596> , 2004.
- 830 Laskin, A., Wietsma, T. W., Krueger, B. J., and Grassian, V. H.: Heterogeneous chemistry of individual  
831 mineral dust particles with nitric acid: A combined CCSEM/EDX, ESEM, and ICP-MS study, *Journal of*  
832 *Geophysical Research: Atmospheres*, 110(D10), <https://doi.org/10.1029/2004JD005206> , 2005.
- 833 Li, J., Wang, W.-C., Liao, H., and Chang, W.: Past and future direct radiative forcing of nitrate aerosol in  
834 East Asia, *Theoretical and Applied Climatology*, 121, 445-458, [https://doi.org/10.1007/s00704-014-](https://doi.org/10.1007/s00704-014-1249-1)  
835 [1249-1](https://doi.org/10.1007/s00704-014-1249-1) , 2015.
- 836 Liao, H., Seinfeld, J. H., Adams, P. J., and Mickley, L. J.: Global radiative forcing of coupled tropospheric  
837 ozone and aerosols in a unified general circulation model, *Journal of Geophysical Research:*  
838 *Atmospheres*, 109(D16), <https://doi.org/10.1029/2003JD004456> , 2004.
- 839 Lohmann, U. and Roeckner, E.: Design and performance of a new cloud microphysics scheme developed  
840 for the ECHAM general circulation model, *Climate Dynamics*, 12, 557-572,  
841 <https://doi.org/10.1007/BF00207939> , 1996.
- 842 Lohmann, U. and Feichter, J.: Global indirect aerosol effects: a review, *Atmospheric Chemistry and*  
843 *Physics*, 5(3), <https://doi.org/10.5194/acp-5-715-2005> , 2005.
- 844 Lohmann, U. and Ferrachat, S.: Impact of parametric uncertainties on the present-day climate and on  
845 the anthropogenic aerosol effect, *Atmospheric Chemistry and Physics*, 10(23),  
846 <https://doi.org/10.5194/acp-10-11373-2010> , 2010.
- 847 Milouisis, A., Tsimpidi, A. P., Tost, H., Pandis, S. N., Nenes, A., Kiendler-Scharr, A., and Karydis, V. A.:  
848 Implementation of the ISORROPIA-lite aerosol thermodynamics model into the EMAC chemistry  
849 climate model (based on MESSy v2.55): implications for aerosol composition and acidity,  
850 *Geoscientific Model Development*, 17(3), 1111-1131, <https://doi.org/10.5194/gmd-17-1111-2024> ,  
851 2024.
- 852 Morales Betancourt, R. and Nenes, A.: Understanding the contributions of aerosol properties and  
853 parameterization discrepancies to droplet number variability in a global climate model, *Atmospheric*  
854 *Chemistry and Physics*, 14(9), 4809-4826, <https://doi.org/10.5194/acp-14-4809-2014> , 2014.
- 855 Myhre, G., Samset, B. H., Schulz, M., Balkanski, Y., Bauer, S., Berntsen, T. K., Bian, H., Bellouin, N., Chin,  
856 M., Diehl, T., Easter, R. C., Feichter, J., Ghan, S. J., Hauglustaine, D., Iversen, T., Kinne, S., Kirkevåg, A.,  
857 Lamarque, J. F., Lin, G., Liu, X., Lund, M. T., Luo, G., Ma, X., van Noije, T., Penner, J. E., Rasch, P. J.,  
858 Ruiz, A., Seland, Ø., Skeie, R. B., Stier, P., Takemura, T., Tsigaridis, K., Wang, P., Wang, Z., Xu, L., Yu, H.,  
859 Yu, F., Yoon, J. H., Zhang, K., Zhang, H., and Zhou, C.: Radiative forcing of the direct aerosol effect  
860 from AeroCom Phase II simulations, *Atmospheric Chemistry and Physics*, 13(4), 1853-1877,  
861 <https://doi.org/10.5194/acp-13-1853-2013> , 2013.
- 862 Myhre, G., Shindell, D., and Pongratz, J.: Anthropogenic and natural radiative forcing, *Climate Change*  
863 *2013-The Physical Science Basis*, 659-740, <https://dx.doi.org/10.1017/CBO9781107415324.018> ,  
864 2014.
- 865 Nenes, A., Murray, B., Bougiatioti, A. (2014). Mineral Dust and its Microphysical Interactions with  
866 Clouds. In: Knippertz, P., Stuut, JB. (eds) *Mineral Dust*. Springer, Dordrecht.  
867 [https://doi.org/10.1007/978-94-017-8978-3\\_12](https://doi.org/10.1007/978-94-017-8978-3_12) , 2014.
- 868 Pozzer, A., Jockel, P. J., Sander, R., Williams, J., Ganzeveld, L., and Lelieveld, J.: Technical note: the  
869 MESSy-submodel AIRSEA calculating the air-sea exchange of chemical species, *Atmospheric*  
870 *Chemistry and Physics*, 6(12), 5435-5444, <https://doi.org/10.5194/acp-6-5435-2006> , 2006.



- 871 Pringle, K. J., Tost, H., Message, S., Steil, B., Giannadaki, D., Nenes, A., Fountoukis, C., Stier, P., Vignati, E.,  
872 and Lelieveld, J.: Description and evaluation of GMXe: a new aerosol submodel for global simulations  
873 (v1), *Geoscientific Model Development*, 3(2), <https://doi.org/10.5194/gmd-3-391-2010>, 2010a.
- 874 Pringle, K. J., Tost, H., Metzger, S., Steil, B., Giannadaki, D., Nenes, A., Fountoukis, C., Stier, P., Vignati, E.,  
875 and Lelieveld, J.: Corrigendum to "Description and evaluation of GMXe: a new aerosol submodel for  
876 global simulations (v1)" published in *Geosci. Model Dev.*, 3, 391–412, 2010, *Geoscientific Model  
877 Development*, 3(2), 413–413, <https://doi.org/10.5194/gmd-3-413-2010>, 2010b.
- 878 Roeckner, E., Brokopf, R., Esch, M., Giorgetta, M., Hagemann, S., Kornblüeh, L., Manzini, E., Schlese, U.,  
879 and Schulzweida, U.: Sensitivity of simulated climate to horizontal and vertical resolution in the  
880 ECHAM5 atmosphere model, *Journal of Climate*, 19(16), 3771–3791,  
881 <https://doi.org/10.1175/JCLI3824.1>, 2006.
- 882 Sander, R., Baumgaertner, A., Cabrera-Perez, D., Frank, F., Gromov, S., Grooss, J. U., Harder, H., Huijnen,  
883 V., Jockel, P., Karydis, V. A., Niemeier, K. E., Pozzer, A., Hella, R. B., Schultz, M. G., Taraborrelli, D.,  
884 and Tauer, S.: The community atmospheric chemistry box model CAABA/MECCA-4.0, *Geoscientific  
885 Model Development*, 12(4), 1365–1385, <https://doi.org/10.5194/gmd-12-1365-2019>, 2019.
- 886 Seinfeld, J. H. and Pandis, S. N.: *Atmospheric chemistry and physics from air pollution to climate change*,  
887 John Wiley & Sons, ISBN 1118947401, 2016.
- 888 Seinfeld, J. H., Bretherton, C., Carslaw, K. S., Coe, H., DeMott, P. J., Dunlea, E. J., Feingold, G., Ghan, S.,  
889 Guenther, A. B., Kahn, R., Kraucunas, I., Kreidenweis, S. M., Molina, M. J., Nenes, A., Penner, J. E.,  
890 Prather, K. A., Ramanathan, V., Ramaswamy, V., Rasch, P. J., Ravishankara, A. R., Rosenfeld, D.,  
891 Stephens, G., and Wood, R.: Improving our fundamental understanding of the role of aerosol–cloud  
892 interactions in the climate system, *Proceedings of the National Academy of Sciences*, 113(21), 5781–  
893 5790, <https://doi.org/10.1073/pnas.1514043113>, 2016.
- 894 Sposito, G.: *The Chemistry of Soils*, Oxford University Press, New York, ISBN 9780190630881, 1989.
- 895 Sundqvist, H., Berge, E., and Kristjánsson, J. E.: Condensation and Cloud Parameterization Studies with a  
896 Mesoscale Numerical Weather Prediction Model, *Monthly Weather Review*, 117(8), 1641–1657,  
897 [https://doi.org/10.1175/1520-0493\(1989\)117%3C1641:CACPSW%3E2.0.CO;2](https://doi.org/10.1175/1520-0493(1989)117%3C1641:CACPSW%3E2.0.CO;2), 1989.
- 898 Tompkins, A. M.: A Prognostic Parameterization for the Subgrid-Scale Variability of Water Vapor and  
899 Clouds in Large-Scale Models and Its Use to Diagnose Cloud Cover, *Journal of the Atmospheric  
900 Sciences*, 59(12), 1917–1942, [https://doi.org/10.1175/1520-  
901 0469\(2002\)059%3C1917:APPFTS%3E2.0.CO;2](https://doi.org/10.1175/1520-0469(2002)059%3C1917:APPFTS%3E2.0.CO;2), 2002.
- 902 Tost, H., Jockel, P. J., Kerkweg, A., Sander, R., and Lelieveld, J.: Technical note: A new comprehensive  
903 SCAVenging submodel for global atmospheric chemistry modelling, *Atmospheric Chemistry and  
904 Physics*, 6(3), 565–574, <https://doi.org/10.5194/acp-6-565-2006>, 2006.
- 905 Tost, H., Jöckel, P., and Lelieveld, J.: Lightning and convection parameterisations - uncertainties in global  
906 modelling, *Atmospheric Chemistry and Physics*, 7(17), 4553–4568, [https://doi.org/10.5194/acp-7-  
907 4553-2007](https://doi.org/10.5194/acp-7-4553-2007), 2007a.
- 908 Tost, H., Jockel, P., Kerkweg, A., Pozzer, A., Sander, R., and Lelieveld, J.: Global cloud and precipitation  
909 chemistry and wet deposition: tropospheric model simulations with ECHAM5/MESy1, *Atmospheric  
910 Chemistry and Physics*, 7(10), 2733–2757, <https://doi.org/10.5194/acp-7-2733-2007>, 2007b.
- 911 Trump, E. R., Fountoukis, C., Donahue, N. M., and Pandis, S. N.: Improvement of simulation of fine  
912 inorganic PM levels through better descriptions of coarse particle chemistry, *Atmospheric  
913 Environment*, 102, 274–281, <https://doi.org/10.1016/j.atmosenv.2014.11.059>, 2015.
- 914 Tsigaridis, K. and Kanakidou, M.: The present and future of secondary organic aerosol direct forcing on  
915 climate, *Current Climate Change Reports*, 4, 84–98, <https://doi.org/10.1007/s40641-018-0092-3>,  
916 2018.



- 917 Twomey, S.: The Influence of Pollution on the Shortwave Albedo of Clouds, *Journal of Atmospheric*  
918 *Sciences*, 34, 1149-1152, [https://doi.org/10.1175/1520-0469\(1977\)034%3C1149:TIOPOT%3E2.0.CO;2](https://doi.org/10.1175/1520-0469(1977)034%3C1149:TIOPOT%3E2.0.CO;2)  
919 , 1977.
- 920 Urdiales-Flores, D., Zittis, G., Hadjinicolaou, P., Osipov, S., Klingmüller, K., Mihalopoulos, N., Kanakidou,  
921 M., Economou, T., and Lelieveld, J.: Drivers of accelerated warming in Mediterranean climate-type  
922 regions, *npj Climate and Atmospheric Science*, 6(1), 97, <https://doi.org/10.1038/s41612-023-00423-1>  
923 , 2023.
- 924 Vignati, E., Wilson, J., and Stier, P.: M7: An efficient size-resolved aerosol microphysics module for large-  
925 scale aerosol transport models, *Journal of Geophysical Research: Atmospheres*, 109(D22),  
926 <https://doi.org/10.1029/2003JD004485> , 2004.
- 927 Wong, J. P. S., Tsagkaraki, M., Tsiadra, I., Mihalopoulos, N., Violaki, K., Kanakidou, M., Sciare, J., Nenes,  
928 A., and Weber, R. J.: Atmospheric evolution of molecular-weight-separated brown carbon from  
929 biomass burning, *Atmospheric Chemistry and Physics*, 19(11), 7319-7334,  
930 <https://doi.org/10.5194/acp-19-7319-2019> , 2019.
- 931 Xu, L. and Penner, J. E.: Global simulations of nitrate and ammonium aerosols and their radiative effects,  
932 *Atmospheric Chemistry and Physics*, 12(20), <https://doi.org/10.5194/acp-12-9479-2012> , 2012.
- 933 Yienger, J. J. and Levy, H.: EMPIRICAL-MODEL OF GLOBAL SOIL-BIOGENIC NOX EMISSIONS, *Journal of*  
934 *Geophysical Research: Atmospheres*, 100(D6), <https://doi.org/10.1029/95JD00370> , 1995.
- 935 Zhang, Y., Forrister, H., Liu, J., Dibb, J., Anderson, B., Schwarz, J. P., Perring, A. E., Jimenez, J. L.,  
936 Campuzano-Jost, P., Wang, Y., Nenes, A., and Weber, R. J.: Top-of-atmosphere radiative forcing  
937 affected by brown carbon in the upper troposphere, *Nature Geoscience*, 10(7),  
938 <https://doi.org/10.1038/ngeo2960> , 2017.
- 939 Zhang, B.: The effect of aerosols to climate change and society, *Journal of Geoscience and Environment*  
940 *Protection*, 8(08), 55, <https://doi.org/10.4236/gep.2020.88006> , 2020.
- 941
- 942